The Journal of Chemical Physics

A multireference coupled-electron pair approximation combined with complete-active space perturbation theory in local pair-natural orbital framework

Cite as: J. Chem. Phys. **152**, 114111 (2020); https://doi.org/10.1063/1.5142622
Submitted: 15 December 2019 . Accepted: 01 March 2020 . Published Online: 18 March 2020

Masaaki Saitow, and Takeshi Yanai

The Journal of Chemical Physics ARTICLE scitation.org/journal/jcp

A multireference coupled-electron pair approximation combined with complete-active space perturbation theory in local pair-natural orbital framework

Cite as: J. Chem. Phys. 152, 114111 (2020); doi: 10.1063/1.5142622
Submitted: 15 December 2019 • Accepted: 1 March 2020 •
Published Online: 18 March 2020

Masaaki Saitow[1,a] and Takeshi Yanai[1,2,3]

AFFILIATIONS

[1] Department of Chemistry, Graduate School of Science, Nagoya University, Furocho, Chikusa Ward, Nagoya, Aichi 464-8601, Japan
[2] Institute of Transformative Bio-Molecules (WPI-ITbM), Nagoya University, Furocho, Chikusa Ward, Nagoya, Aichi 464-8601, Japan
[3] Japan Science and Technology Agency, PRESTO, 4-1-8 Honcho, Kawaguchi, Saitama 332-0012, Japan

[a] **Author to whom correspondence should be addressed:** msaitow514@gmail.com

ABSTRACT

The Complete-Active Space Second-order Perturbation Theory (CASPT2) has been one of the most widely-used methods for reliably calculating electronic structures of multireference systems. Because of its lowest level treatment of dynamic correlation, it has a high computational feasibility; however, its accuracy in some cases falls short of needs. Here, as a simple yet higher-order alternative, we introduce a hybrid theory of the CASPT2 and a multireference variant of the Coupled-Electron Pair Approximation (CEPA), which is a class of high level correlation theory. A central feature of our theory (CEPT2) is to use the two underlying theories for describing different divisions of correlation components based on the full internal contraction framework. The external components, which usually give a major contribution to the dynamic correlation, are intensively described using the CEPA *Ansatz*, while the rests are treated at the CASPT2 level. Furthermore, to drastically reduce the computational demands, we have incorporated the pair-natural orbital (PNO) method into our multireference implementations. This development, thus, requires highly complex derivations and coding, while it has been largely facilitated with an automatic expression and code generation technique. To highlight the accuracy of the CEPT2 approach and to assess the errors caused by the PNO truncation, benchmark calculations are shown on small- to medium-size molecules, illustrating the high accuracy of the present CEPT2 model. By tightening the truncation thresholds, the PNO-CEPT2 energy converges toward the canonical counterpart and is more accurate than that of PNO-CASPT2 as long as the same truncation thresholds are used.

I. INTRODUCTION

Electronic structures that cannot be well approximated by a single Slater determinant are common in chemistry. An electronic wave function of the low-spin open-shell states where there are multiple anti-ferromagnetically coupled electrons is a very typical example of such cases.[1] The electron correlation effect that plays an important role in these problems is often referred to as static correlation.[2] However, to obtain quantitative accuracy, it is often necessary to consider dynamic correlation, which is the remaining component of the correlation effect. The most straightforward way to take into account both types of correlations in a well-balanced manner is the multireference (MR) wave function theories[3–5] that are based on the multiconfigurational self-consistent field (CASSCF) reference

function.[6–8] Note that there are tremendous attempts to utilize the single-reference (SR) framework[9–18] for capturing the static correlation effect.

Among the MR wave function theories, the Complete-Active Space Second-order Perturbation Theory (CASPT2) pioneered by Roos and co-workers[19,20] in the early 1990s has been widely used as a fundamental tool for achieving quantitative accuracy for systems of the complicated electronic structure including organic molecules of doubly excited nature[21] and mono-[22,23] and multi-nuclear[24,25] transition metal complexes. This high feasibility stems from its lowest perturbative treatment of dynamic correlation; however, its PT2 level accuracy in some cases falls short of needs. In addition, the CASPT2 potential energy surface can often suffer from singularity due to the near degeneracy, especially if the active space is too small; this particular issue associated with the CASPT2 model is known as the intruder state problem. There have been several regularization techniques proposed in order to remedy this issue, including real[26] and imaginary[27] shifts. A newer variant of CASPT called N-Electron Valence-state Perturbation Theory (NEVPT) was proposed by Angeli *et al.*[28–30] using Dyall's zeroth-order Hamiltonian[31] to overcome some of the shortcomings of the CASPT approach. As both approaches converge to the conventional second-order Møller–Plesset (MP2) perturbation theory[32] in the closed-shell SR limit, floating-point operations (FPOs) needed to calculate CASPT2 and NEVPT2 energies scale at least as $O(N_c^2 N_v^2)$ for a system with a fixed number of active molecular orbitals (MOs), where N_c and N_v represent the numbers of doubly occupied and virtual MOs, respectively. Before calculating the CASPT2 energy, one has to solve the first-order amplitude equations and, hence, the memory or storage requirement also scales as $O(N_c^2 N_v^2)$. For a system with more active MOs, the prefactors of both memory and FPO requirements steeply increase because their working equations involve the reduced-density matrices (RDMs) of up to four-body nature whose size scales as $O(N_a^8)$, with N_a being the number of active MOs. Therefore, routine application of CASPT2 methods to systems with more than 1000 atomic orbital (AO) functions often becomes prohibitively expensive.

To improve the applicability of the CASPT2 approach, numerous efforts have been made including the use of frozen-natural orbitals (FNOs)[33,34] in the virtual space in conjunction with the Cholesky decomposition technique for reducing the costs of MO integral transformation[35–38] and of the tensor-hypercontraction (THC) technique.[39] The density-fitting (DF) or resolution-of-the-identity (RI) approximation has also been used for accelerating CASPT2 computation.[40] Recently, Katz and Werner developed a CASPT2 approach in the so-called pair-natural orbital (PNO) framework, which has been coined PNO-CASPT2, and demonstrated its applicability to large, real-life MR systems composed of up to approximately 3000 AO functions.[41,42]

The original concept of PNOs was already realized in the 1960s in order to accelerate the convergence of the configuration interaction (CI) expansions.[43–49] Importantly, the PNO-based MRCI theory and the MR Coupled-Electron Pair Approximation (PNO-MCCEPA) using internally contracted (IC) configuration functions were developed by Taylor[50] and Fink and Staemmler,[51] respectively.

The use of PNOs in the context of modern wave function theories was first introduced by Neese and co-workers in their local PNO-based CEPA (LPNO-CEPA)[52] and Coupled-Cluster (LPNO-CCSD)[53–55] methods implemented in the Orca package.[56] The LPNO-CEPA/CCSD is applicable to systems composed of up to 2000 AO bases, which is far beyond the reach of the canonical counterpart while recovering almost 99.9% of the canonical correlation energy. Later, they have developed a more sophisticated variant called domain-based LPNO-CC (DLPNO-CC) methods for large, real-life systems involving hundreds of atoms and thousands of AO functions.[57–62] The DLPNO scheme has been extended to MR wave function theories, resulting in the DLPNO-MR-CC method based on Mukherjee's state-specific formalism[63–65] and the DLPNO-NEVPT2 method.[66] In a similar vein, variants of PNO-based reduced-scaling wave function methods have been developed by many research groups including PNO-LCC methods by Werner *et al.*[67–73] and a variant of the PNO-CC method and PNO-based theories for the excited states by Hättig *et al.*[74–82]

The internally contracted basis (ICB) functions spanning the first-order interacting space (FOIS) are classified into three types according to their excitation characters: Those configurations with single and double excitations into the virtual space are called semi-internal and external, respectively. The remaining IC configurations, which do not involve any excitations into the virtual space, are labeled internal. In the closed-shell SR limit, the external configurations converge simply to the doubly excited configurations, while all the remaining configurations vanish. In the general MR cases, actually, the semi-internal and internal IC configurations involve not only simple single-excitations but also the pseudo-double excitations because some of the active MOs may possess occupation number very close to zero. Actually, in the 1980s, Roos *et al.* developed a primitive version of CASPT2 that involves only the external IC configurations[83] and, as summarized in Ref. 84, reported that the semi-internal subspaces in FOIS can have a large impact on the dynamic correlation energy. Note that the first version of IC-MR-CC theory proposed by Banerjee and Simons also lacks the important semi-internal components in the wave function.[85]

In this paper, we report a hybrid of IC-MR-CEPA and CASPT2 methods, which is coined the CEPT2 approach, as a higher-order, yet simple, extension to the conventional CASPT2 method for capturing more dynamic correlation effects. The external configurations in the first-order CEPT wave function are treated at the IC-MR-CEPA level, while the remaining semi-internal and internal configurations are kept at the CASPT2 level. The coupling between two *Ansätze* has been accomplished in a similar vein to the CIPT2 model by Werner and co-workers.[86] In the closed-shell SR limit, the CEPT2 model converges to the Linearized Coupled-Cluster Doubles (L-CCD) or, equivalently, the CEPA/0 Doubles [CEPA/0(D)] that recover more dynamic correlation energy than the MP2 model. Note that Fink and co-workers proposed a variant of MR perturbation theory[87–89] that also converges to the L-CCD or CEPA/0(D) model in the closed-shell SR limit at the second-order level and is known as the so-called Retention-of-Excitation-degree Perturbation Theory (REPT).

In the original CIPT2 model,[90,91] the reference configurations and all the excited configurations involving excitations solely from the active MO space are treated at the MRCI level while leaving the remaining ones at the CASPT2 level in order to remedy the intruder state problems without employing any empirical level shifts.

Actually, treating those configurations in the IC framework at the MRCI level is known to cause several computational difficulties, the most severe one of which is the appearance of 5-RDMs.[92] An active space 5-RDM is a tensor quantity associated with 10 active MO indices, and hence, those systems with 16 active MOs generation and storage of the 5-RDM require more than 8.0 terabytes of disk space. Therefore, in the partially IC-MRCI models[91,93] implemented in the Molpro package,[94] such configurations are decontracted to remove them from the working equations.

Later, by rewriting the Hamiltonian matrix element into a commutator-based expression as done in the NEVPT2 formalism,[28] the MRCI theory in a fully IC framework (FIC-MRCI) without 5-RDM was formulated.[95–98] However, tensor contractions involving the 4-RDM and the t-amplitude in the FIC-MRCI σ-equation can still be a bottleneck even for systems with a relatively small active space as their computational scaling is of $O(N_c N_a^8)$, $O(N_a^9)$, or $O(N_a^8 N_v)$. In the CEPT2 model, on the other hand, such contractions do not appear in the residua and all the 4-RDMs are contracted to the Fock operator, thus appearing as an effective 3-body tensor with $O(N_a^8)$ costs just as in the case of the conventional CASPT2. Such a Fock-contracted 4-RDM can be pre-computed only once in a CEPT2 energy computation, while in the FIC-MRCI, the t-contracted 4-RDM should be constructed in each iteration for the diagonalization of the Hamiltonian matrix.

Even though the full IC-MR-CEPA/0 lacks size-consistency, all the CEPA terms introduced are fully connected, and thus, the near-size-consistent nature of CASPT2 is directly inherited to the CEPT2 model. The use of MR-CEPA *Ansatz* for the external subspaces introduces several terms involving 4-external MO integrals contracted to the t-amplitude, which may potentially make the whole computation quite demanding even for relatively small systems. These types of contraction terms are often referred to as the 4-External Exchange Operators (4-EEOs) and are known to be the most expensive terms in the SR-CEPA and CCSD computations with $O(N_c^2 N_v^4)$ computational costs. To overcome this issue, we introduce PNO expansion in the external subspace in a similar vein to Ref. 41. Derivation and implementation of our PNO-CASPT2/CEPT2 scheme have been achieved by an automatic code generation framework, which was used in our previous works[95,96] and has been extended to handle PNOs.

This paper proceeds as follows: In Sec. II, we show how the PNOs are defined in the MR cases and used in the CASPT2 formalism. The PNO-CEPT2 *Ansatz* is given as an extension to the PNO-CASPT2 model, and the strategy we have chosen to use for the automatic code generation in the PNO framework is addressed. In Sec. III, the accuracy of the canonical CEPT2 model and the PNO truncation errors are validated for N_2 dissociation. The isomerization energy profile of the $[Cu_2O_2]^{2+}(NH_3)_6$ complex calculated at the PNO-CEPT2 level of theory is shown and compared to that by the CASPT2 and the previous theoretical results. The excitation energies (EEs) for the dipole-accessible and dipole-forbidden states of butadiene and longer polyene chains calculated by the PNO-CEPT2 theory are given and compared to the experimental and other theoretical values. The accuracy of the PNO-CEPT2 model is examined by using various PNO truncation thresholds in calculating the Singlet–Triplet energy (S–T) gap for the free-base porphyrin. In Sec. IV, conclusions are drawn.

II. THEORY

A. Notations and convention

Throughout this paper, we use *ijkl*..., *pqrs*..., and *abcd*... to represent the doubly occupied, active, and virtual MOs, respectively, while the generic MOs are indicated by *wxyz*.... The derivation and implementation of the working equations of the PNO-CEPT approach are based on the reduced spin-free excitation operators[99–102]

$$E_x^w = \sum_{\sigma=\{\alpha,\beta\}} a^{w\sigma} a_{x\sigma}, \tag{1}$$

$$E_{yz}^{wx} = \sum_{\sigma,\tau=\{\alpha,\beta\}} a^{w\sigma} a^{x\tau} a_{z\tau} a_{y\sigma}, \tag{2}$$

where a^w (a_w) represents the Fermionic creation (annihilation) operator that acts on the wth spatial MO. By using Eqs. (1) and (2), the Born–Oppenheimer (BO) Hamiltonian is given as

$$H = \sum_{wx} h_{wx} + \frac{1}{2} \sum_{wxyz} (wy|xz) E_{yz}^{wx}, \tag{3}$$

where h_{wx} and $(wy|xz)$ are one- and two-electron integrals, respectively. The redundant internally contracted basis (r-ICB) functions that span the first-order interacting space (FOIS) are generated by applying the following eight types of excitation operators to the reference CASSCF wave function ($|\Psi_0\rangle$):

$$E_{ij}^{ab},\ E_{pi}^{ab},\ E_{pq}^{ab} \tag{4}$$

for the external subspaces,

$$\{E_{ip}^{aq},\ E_{ip}^{qa}\},\ E_{ij}^{pa},\ E_{pq}^{ra} \tag{5}$$

for the semi-internal subspaces, and

$$E_{ij}^{pq},\ E_{ip}^{qr} \tag{6}$$

for the internal subspaces. The energy and residual equations involve an expectation value of a string of E-operators with respect to the reference such as $\langle\Psi_0|E_{ab}^{pq}E_{wx}^{yz}\cdots|\Psi_0\rangle$. Such an expectation value is evaluated by invoking Wick's theorem for the E-operators and is reduced to a reduced-density matrix (RDM) composed only of active MO indices,

$$D_q^p = \langle\Psi_0|E_q^p|\Psi_0\rangle, \tag{7}$$

$$D_{rs}^{pq} = \langle\Psi_0|E_{rs}^{pq}|\Psi_0\rangle. \tag{8}$$

The r-ICB functions are a non-orthonormal and linearly dependent set of functions as a basis of FOIS. Therefore, the amplitude equations of MR wave function methods are solved in the linearly independent and orthonormalized IC representation spanned by the non-redundant (nr-) ICB functions

$$|\Psi_{ij}^{ab}\rangle,\ |\Psi_{\rho i}^{ab}\rangle,\ |\Psi_{\rho}^{ab}\rangle \tag{9}$$

for the external subspaces,

$$|\Psi^a_{\rho i}\rangle,\ |\Psi^{\rho a}_{ij}\rangle,\ |\Psi^a_\rho\rangle \tag{10}$$

for the semi-internal subspaces, and

$$|\Psi^\rho_{ij}\rangle,\ |\Psi_{i\rho}\rangle \tag{11}$$

for the internal subspaces, where $\rho\tau\ldots$ are used to represent the eigenvectors of metric for each subspace [Eqs. (4)–(6)].

B. Brief summary of PNO-CASPT2 algorithm

As we follow a similar vein to the original formalism by Katz and Werner,[41,42] we only outline the PNO-CASPT2 theory in this section. In the original CASPT2 formalism, the following zeroth-order Hamiltonian is used:

$$H_0 = \mathscr{P}_0 F \mathscr{P}_0 + \mathscr{P}_{0^\perp} F \mathscr{P}_{0^\perp} + \mathscr{P}_{\mathrm{FOIS}} F \mathscr{P}_{\mathrm{FOIS}} + \cdots, \tag{12}$$

with $\mathscr{P}$ being the projection operators onto each subspace in a Hilbert space,

$$\mathscr{P}_0 = |\Psi_0\rangle\langle\Psi_0|, \tag{13}$$

$$\mathscr{P}_{0^\perp} = \sum_{\mu\in\{0^\perp\}} |\Psi_\mu\rangle\langle\Psi_\mu|, \tag{14}$$

$$\mathscr{P}_{\mathrm{FOIS}} = \sum_{\mu\in\{\mathrm{FOIS}\}} |\Psi_\mu\rangle\langle\Psi_\mu|, \tag{15}$$

where the $\{0^\perp\}$ represents an orthogonal complement of the reference space.

In Eq. (12), the generalized Fock operator reads

$$F = \sum_{wx} f_{wx} E^x_w, \tag{16}$$

where f represents the generalized Fock matrix

$$f_{wx} = (f_{\mathrm{core}})_{wx} + \sum_{pq}\left[(wx|pq) - \frac{1}{2}(wp|xq)\right] D^p_q, \tag{17}$$

$$(f_{\mathrm{core}})_{wx} = h_{wx} + \sum_i [2(wx|ii) - (wi|xi)]. \tag{18}$$

The PNO-CASPT2 wave function is defined as

$$\begin{aligned}|\Psi\rangle = &\sum_{ij}\sum_{a_{ij}b_{ij}} t^{ij}_{a_{ij}b_{ij}} |\Psi^{a_{ij}b_{ij}}_{ij}\rangle + \sum_{\rho i}\sum_{a_{\rho i}b_{\rho i}} t^{\rho i}_{a_{\rho i}b_{\rho i}} |\Psi^{a_{\rho i}b_{\rho i}}_{\rho i}\rangle + \sum_{\rho}\sum_{a_\rho b_\rho} t^{\rho}_{a_\rho b_\rho} |\Psi^{a_\rho b_\rho}_{\rho}\rangle \\ &+ \sum_{\rho ij}\sum_{a_{ij}} t^{ij}_{\rho a_{ij}} |\Psi^{\rho_{ij} a}_{ij}\rangle + \sum_{\rho i}\sum_a t^{\rho i}_a |\Psi^a_{\rho i}\rangle + \sum_\rho \sum_a t^\rho_a |\Psi^a_\rho\rangle \\ &+ \sum_{\rho ij} t^{ij}_\rho |\Psi^\rho_{ij}\rangle + \sum_{\rho i} t^i_\rho |\Psi^\rho_i\rangle\end{aligned} \tag{19}$$

using the nr-ICB functions that are constructed by orthonormalizing and canonicalizing the redundant counterparts. Canonicalization of the ICBs over diagonalizing the active space part of the zeroth-order Hamiltonian plays an important role in the canonical CASPT2 theory. For instance, an nr-ICB with double excitations to the active space, $\{\Psi^\rho_{ij}\}$, is related to its redundant counterpart as

$$|\Psi^\rho_{ij}\rangle = \sum_{pq} C^\rho_{pq} |\tilde{\Psi}^{pq}_{ij}\rangle = \sum_{pq} C^\rho_{pq} E^{pq}_{ij} |\Psi_0\rangle, \tag{20}$$

where the orthonormalization matrix, $\mathbf{C}$, is obtained by solving the generalized eigenvalue problem,

$$\sum_{rs}\langle\Psi_0|E^{ij}_{pq} F E^{rs}_{ij}|\Psi_0\rangle C^\rho_{rs} = E_{\rho ij}\sum_{rs}\langle\Psi_0|E^{ij}_{pq}E^{rs}_{ij}|\Psi_0\rangle C^\rho_{rs}. \tag{21}$$

The PNO-CASPT2 amplitudes are determined by solving the residual equations,

$$\begin{aligned} r^I &= \frac{\partial}{\partial t^I}\mathscr{F}_{\text{PNO-CASPT2}} \\ &= \sum_J \langle\Psi^I|F - \langle F\rangle|\Psi_J\rangle t^J + \langle\Psi^I|H|\Psi_0\rangle \to 0, \end{aligned} \tag{22}$$

where IJ represent one of the eight non-redundant subspaces of FOIS. The Hylleraas-type energy functional for PNO-CASPT2 *Ansatz* is given as

$$\mathscr{F}_{\text{PNO-CASPT2}} = \langle\Psi|H|\Psi_0\rangle + \langle\Psi_0|H|\Psi\rangle + \langle\Psi|F - \langle F\rangle|\Psi\rangle. \tag{23}$$

The amplitudes in the r-ICB representation ($\tilde{\mathbf{t}}$) can be obtained by back-transforming the nr-ICB counterpart ($\mathbf{t}$) as

$$\tilde{t}^{pq}_{ij} = \sum_\rho C^\rho_{pq} t^\rho_{ij}. \tag{24}$$

In the typical canonical CASPT2 implementation, the residua that correspond to Eq. (22) are evaluated in r-ICB representation using the $\tilde{\mathbf{t}}$ amplitudes and then transformed into the nr-ICB representation as

$$r^\rho_{ij} = \sum_\rho C^\rho_{pq} \tilde{r}^{pq}_{ij} \tag{25}$$

for the $\{\Psi^\rho_{ij}\}$ subspace.

In Eq. (19), the PNOs are introduced only in the external subspaces and a semi-internal subspace spanned by the $\{\Psi^{\rho a_{ij}}_{ij}\}$ function. Since the PNOs for $\{\Psi^{a_\rho b_\rho}_\rho\}$ and $\{\Psi^{a_{\rho i} b_{\rho i}}_{\rho i}\}$ subspaces are dependent not only on the localized doubly occupied MOs but also on the nr-ICB functions, in the PNO-CASPT2 implementation, one cannot back transform the external amplitudes ($\mathbf{t}$) and the residua ($\mathbf{r}$) into the r-ICB representation while taking the advantage of compactness of the PNO space. Therefore, in our PNO-CASPT2 implementation, we do not perform any back-transformation into the r-ICB representation and the residua are constructed directly in the nr-ICB representation using the orthonormalized amplitudes. Note that such back-transformation is certainly possible for those subspaces where no PNOs are introduced.

The PNO-CASPT2/CEPT2 computation begins by localizing the doubly occupied MOs by the Pipek–Mezey procedure.[103] Note that the active MOs are not localized in our PNO-CASPT2/CEPT2 scheme.

The PNOs for ij-, ρi-, and ρ-pairs are generated by diagonalizing the pair-densities for the corresponding pairs,

$$(D^{ij})_{ab} = \langle\Psi_{ij}|E^a_b|\Psi_{ij}\rangle \quad (\text{for } \{\Psi^{ab}_{ij}\} \text{ subspace}), \tag{26}$$

$$(D^{\rho i})_{ab} = \langle\Psi_{\rho i}|E^a_b|\Psi_{\rho i}\rangle \quad (\text{for } \{\Psi^{ab}_{\rho i}\} \text{ subspaces}), \tag{27}$$

$$(D^{\rho})_{ab} = \langle\Psi_{\rho}|E^a_b|\Psi_{\rho}\rangle \quad (\text{for } \{\Psi^{ab}_{\rho}\} \text{ subspaces}). \tag{28}$$

For the $\{\Psi_{ij}^{\rho a_{ij}}\}$ subspace, we use the *ij*-PNOs obtained as eigenfunctions of Eq. (26). Those PNOs with smaller occupation numbers than a user-defined threshold (`TCutPNO`) are screened out. The PNO truncation error for a pair is estimated by taking difference between full and truncated semi-local diagonally approximated CASPT2 (SL-CASPT2-D) pair-energies,

$$e_{ij} = \langle \Psi_0 | H | \Psi_{ij} \rangle, \tag{29}$$

$$e_{\rho i} = \langle \Psi_0 | H | \Psi_{\rho i} \rangle, \tag{30}$$

$$e_{\rho} = \langle \Psi_0 | H | \Psi_{\rho} \rangle. \tag{31}$$

In the original PNO-CASPT2 implementation, an additional PNO truncation threshold is introduced, especially, for accurately treating the spatially distant pairs.[67] In their scheme, the ratio between truncated and full SL-CASPT2-D pair energies is ensured to be larger than a given threshold,

$$\frac{e_{ij}^{\mathrm{PNO}}}{e_{ij}} \geq T_{\mathrm{PNO}}^{\mathrm{en}}, \tag{32}$$

which is set to 0.997 by default. In our PNO-CASPT2/CEPT2 implementation, we only utilize the occupation-number-based truncation of PNOs as done in the LPNO/DLPNO scheme by Neese and co-workers.

Moreover, only those pairs with pair-energy larger than a given threshold (`TCutPairs`) proceed to the iterative PNO-CASPT2/CEPT2 step. The SL-CASPT2-D pair-functions are used for defining the pair-densities,

$$|\Psi_{ij}\rangle = \sum_{ab} \frac{(ia|jb)}{F_{ii} + F_{jj} - \epsilon_a - \epsilon_b} E_{ij}^{ab} |\Psi_0\rangle, \tag{33}$$

$$|\Psi_{\rho i}\rangle = \sum_{ab} \frac{\langle \Psi_{\rho i}^{ab} | H | \Psi_0 \rangle}{F_{ii} - e_{\rho} - \epsilon_a - \epsilon_b} \sum_{p} C_{p}^{\rho} E_{ip}^{ab} |\Psi_0\rangle, \tag{34}$$

$$|\Psi_{\rho}\rangle = \sum_{ab} \frac{\langle \Psi_{\rho}^{ab} | H | \Psi_0 \rangle}{e_{\rho} - \epsilon_a - \epsilon_b} \sum_{pq} C_{pq}^{\rho} E_{pq}^{ab} |\Psi_0\rangle. \tag{35}$$

The numerators in the SL-CASPT2-D amplitudes involve the 2-external exchange operators (2-EEOs), and hence, this part will be a computational bottleneck in a whole PNO-CASPT2 computation. In our current implementation, we generate a full set of those integrals using the resolution-of-the-identity (RI) approximation[104] and store them on disk. This choice limits the applicability of our PNO-CASPT2 implementation only up to systems composed of not more than 2000 AO functions. To overcome such a difficulty, domain truncation should be introduced in the RI 3-index integral generation and the final 2-EEO construction steps as done in the original PNO-CASPT2 implementations,[41,42] in the DLPNO-CC and NEVPT2 algorithms by Neese and co-workers,[57–62,66,105] and in the PNO-LCC programs by Werner *et al.*[67–69,106]

In the canonical CASPT2 implementation, the nr-ICBs are constructed as eigenfunctions of diagonal blocks of the zeroth-order Hamiltonian by solving the generalized eigenvalue problems akin to Eq. (21) for all the subspaces of FOIS except $\{\Psi_{ij}^{ab}\}$. Therefore, programming the residua [Eq. (22)] of diagonal blocks in the first term is quite simple. However, in the PNO-based counterpart, all the matrix blocks involving at least one doubly occupied MO index should be programmed, leading to a drastic increase in the number of terms that should be derived and programmed. To this end, we extended our code generator framework[95,96,107] such that codes for the PNO-based tensor contractions can also be generated. In our program, the PNO-CASPT2 residual equations are solved by the preconditioned conjugate gradient (PCG) algorithm.

We have also implemented real and imaginary shifts in our PNO-CASPT2 program in the same way as the canonical CASPT2 program. The conventional formulation of the imaginary shifts is based on the diagonality in the diagonal blocks of the zeroth-order Hamiltonian matrix in FOIS, which is not satisfied if the doubly occupied MOs are localized. Therefore, in our PNO-CASPT2 implementation, the off-diagonal elements in the diagonal blocks are discarded, leading to a semi-canonical imaginary shift.

C. The coupled-electron pair perturbation theory

In the PNO-CEPT2 *Ansatz*, we minimize the following energy functional:

$$\mathscr{F}_{\text{PNO-CEPT2}} = \mathscr{F}_{\text{PNO-CEPA/0}}^{\text{ext}} + \mathscr{F}_{\text{PNO-CASPT2}} - \mathscr{F}_{\text{PNO-CASPT2}}^{\text{ext}}, \tag{36}$$

$$\mathscr{F}_{\text{PNO-CEPA/0}}^{\text{ext}} = \langle \Psi^{\text{ext}} | H - E_0 | \Psi^{\text{ext}} \rangle, \tag{37}$$

$$\mathscr{F}_{\text{PNO-CASPT2}}^{\text{ext}} = \langle \bar{\Psi}^{\text{ext}} | H | \Psi_0 \rangle + \langle \Psi_0 | H | \bar{\Psi}^{\text{ext}} \rangle + \langle \bar{\Psi}^{\text{ext}} | F - \langle F \rangle | \bar{\Psi}^{\text{ext}} \rangle, \tag{38}$$

where $\bar{\Psi}^{\text{ext}}$ represents the external part of the wave function,

$$|\Psi^{\text{ext}}\rangle = |\Psi_0\rangle + |\bar{\Psi}^{\text{ext}}\rangle = |\Psi_0\rangle + \Bigg[\sum_{ij} \sum_{a_{ij} b_{ij}} t_{a_{ij} b_{ij}}^{ij} |\Psi_{ij}^{a_{ij} b_{ij}}\rangle + \sum_{\rho i} \sum_{a_{\rho i} b_{\rho i}} t_{a_{\rho i} b_{\rho i}}^{\rho i} |\Psi_{\rho i}^{a_{\rho i} b_{\rho i}}\rangle + \sum_{\rho} \sum_{a_{\rho} b_{\rho}} t_{a_{\rho} b_{\rho}}^{\rho} |\Psi_{\rho}^{a_{\rho} b_{\rho}}\rangle \Bigg]. \tag{39}$$

By defining the remaining semi-internal and internal part of the wave function as

$$|\Psi\rangle = |\Psi_0\rangle + |\bar{\Psi}_{\text{int}}\rangle + |\bar{\Psi}_{\text{ext}}\rangle, \tag{40}$$

the PNO-CEPT2 energy functional [Eq. (36)] reads

$$\begin{aligned} \mathscr{F}_{\text{PNO-CEPT2}} = {} & \langle \bar{\Psi}^{\text{ext}} | H | \Psi_0 \rangle + \langle \Psi_0 | H | \bar{\Psi}^{\text{ext}} \rangle + \langle \bar{\Psi}^{\text{int}} | H | \Psi_0 \rangle \\ & + \langle \Psi_0 | H | \bar{\Psi}^{\text{int}} \rangle + \langle \bar{\Psi}^{\text{ext}} | H - E_0 | \bar{\Psi}^{\text{ext}} \rangle \\ & + \langle \bar{\Psi}^{\text{int}} | F - \langle F \rangle | \bar{\Psi}^{\text{ext}} \rangle + \langle \bar{\Psi}^{\text{ext}} | F - \langle F \rangle | \bar{\Psi}^{\text{int}} \rangle \\ & + \langle \bar{\Psi}^{\text{int}} | F - \langle F \rangle | \bar{\Psi}^{\text{int}} \rangle. \end{aligned} \tag{41}$$

The use of Eq. (36) indicates that the external (Ψ^{ext}) and remaining components in the dynamic correlation energy are

treated at the PNO-CEPA/0 and PNO-CASPT2 levels, respectively. In addition, all the coupling contributions between the external and other subspaces are also treated at the CASPT2 level. By differentiating the above functional with respect to the amplitudes, one obtains the PNO-CEPT2 residual equations as

$$r^E = \langle \Psi^E|H|\Psi_0\rangle + \sum_{E'}\langle \Psi_E|H - E_0|\Psi_{E'}\rangle t^{E'} + \sum_{A}\langle \Psi_E|F|\Psi_A\rangle t^A \to 0, \tag{42}$$

$$r^A = \langle \Psi^A|H|\Psi_0\rangle + \sum_{E}\langle \Psi_A|F|\Psi_E\rangle t^E + \sum_{A'}\langle \Psi_A|F - \langle F\rangle|\Psi_{A'}\rangle t^{A'} \to 0, \tag{43}$$

where $\{E\}$ and $\{A\}$ represent the external and remaining subspaces in FOIS, respectively,

$$\{E\} = \{\Psi_{ij}^{a_{ij}b_{ij}}\} \cup \{\Psi_{i\rho}^{a_{i\rho}b_{i\rho}}\} \cup \{\Psi_{\rho}^{a_\rho b_\rho}\}, \tag{44}$$

$$\{A\} = \{\Psi_{ij}^{\rho a}\} \cup \{\Psi_{\rho i}^{a}\} \cup \{\Psi_{\rho}^{a}\} \cup \{\Psi_{ij}^{\rho}\} \cup \{\Psi_{i}^{\rho}\}. \tag{45}$$

If one evaluates the diagonal block of $\{\Psi_\rho^{a_\rho b_\rho}\}$ subspace straightforwardly using Wick's theorem, there are two terms involving 4-body RDM whose size is approximately 32 GB for systems composed of 16 active MOs. To eliminate such expensive contractions, we employ a commutator-based transformation originally proposed by Angeli and co-workers,[28–30]

$$\begin{aligned} r^\rho_{a_\rho b_\rho} &= \sum_\tau \sum_{c_\tau d_\tau} \langle \Psi^\rho_{a_\rho b_\rho}|H - E_0|\Psi_\tau^{c_\tau d_\tau}\rangle t^\tau_{c_\tau d_\tau} \\ &= \sum_\tau \sum_{c_\tau d_\tau} \sum_{pqrs} C^\rho_{rs}\langle \Psi_0|E^{rs}_{a_\rho b_\rho}(H - E_0)E^{c_\tau d_\tau}_{pq}|\Psi_0\rangle C^\tau_{rs} t^\tau_{c_\tau d_\tau} \\ &= \sum_\tau \sum_{c_\tau d_\tau} \sum_{pqrs} C^\rho_{rs}\langle \Psi_0|E^{rs}_{a_\rho b_\rho}[H, E^{c_\tau d_\tau}_{pq}]|\Psi_0\rangle C^\tau_{rs} t^\tau_{c_\tau d_\tau}, \end{aligned} \tag{46}$$

as we have also utilized in our previous works for developing approximated FIC-MRCI variants with an *ab initio* Density Matrix Renormalization Group (DMRG) reference function.[95,96] Note that both the CEPT2 and CIPT2[86] methods use the energy functional of the similar form. The only difference between them consists in the choice of the CEPA (or MRCI) subspaces; in the CEPT2 *Ansatz*, the external IC configurations are treated at the CEPA level, while in the CIPT2 method, the CEPA or CISD functional is used for those subspaces involving the excitations solely from the active MO space, i.e., $\{\Psi_0\}$, $\{\Psi_\rho^{ab}\}$ and $\{\Psi_\rho^a\}$. To the best of our knowledge, the original CIPT2 theory is based on the partially IC-MRCI formulation and, hence, the reference subspace ($\{\Psi_0\}$) is also decontracted and re-optimized at the CEPA or MRCI level.

The second term in Eq. (42) involves contractions of the 4-EEO with the 2-external amplitude, which are known as the most expensive terms in the canonical CC or CEPA implementations. However, such terms are typically not a bottleneck anymore if the virtual space is spanned by the PNOs. Some of the PNO-CEPA terms involve the semi-joint pair–pair interaction integrals,[52,53] and in the MR case, these terms appear to be more complicated. Apparently, in the SR limit, the PNO-CEPT2 energy and wave function converge to those of PNO-CEPA/0 with Doubles [PNO-CEPA/0(D)] or equivalently PNO-based L-CCD wave function.

All the CEPA terms in Eq. (42) are *linked* in the sense that the amplitude is either directly or indirectly via a 1-body density cumulant connected to the integral. Therefore, as addressed in Ref. 108, even for a super system ($A\cdots B$) composed of infinitely separated two subsystems (A and B), no *unlinked* contractions appear. This indicates that the CEPT2 extension does not violate the near-size-consistent character of the original CASPT2 model.[109]

As we have developed the PNO-CEPT2 code as an extension to our PNO-CASPT2 program, the 2-external nr-ICBs are canonicalizad over diagonalizing the generalized Fock matrix.

Unlike the CIPT2 theory, which is designed to mitigate the intruder state problems typically stemming from the $\{\Psi_i^\rho\}$, $\{\Psi_\rho^a\}$, and the reference subspaces, in the CEPT2 model, we use the CASPT2 *Ansatz* for those subspaces. In the SR case, it is known that the CEPA/0 energy can be irregular, thus showing discontinuity in the potential energy surface. To remedy this drawback, Taube and Bartlett introduced a regularization scheme, which is closely related to the imaginary shift in the CASPT2 framework.[110] Therefore, we have implemented the real- and semi-canonical imaginary shifts and the Hylleraas corrections to minimize the errors caused by such shifts also in the PNO-CEPT2 program.

There are two major differences between the CEPT2 and FIC-REPT2 models. First, in a SR situation, the FIC-REPT2 gives the CEPA/0(D) energy only when all the occupied MOs are included in either of doubly occupied or in the active MO space, while the CEPT2 converges to the CEPA/0(D) energy whenever the reference CASSCF wave function is composed of a single HF configuration. This is because if Fink's zeroth-order Hamiltonian is used all the coupling matrix elements between the external subspaces vanish, thus giving incomplete SR-CEPA/0(D) residua if there are both doubly occupied and active MOs that constitute a single HF reference. Second, in the FIC-REPT2 model, basically all the diagonal matrix blocks of the zeroth-order Hamiltonian appear to be identical to those of the FIC-MR-CEPA/0 and hence the residua involve the expensive t-contracted 4-RDMs.

Our current implementation of the PNO-CEPT2 is still not of optimal form since only the 4-external terms and the 1-body terms, the latter of which are similar to the contractions from $\mathscr{F}^{\text{ext}}_{\text{PNO-CASPT2}}$, are fully evaluated in the PNO space. All the remaining terms from $\mathscr{F}^{\text{ext}}_{\text{PNO-CEPA/0}}$, which involve either 4-internal integrals or semi-joint pair–pair interaction 2-external integral,[52,53] are constructed in the canonical space using the back-transformed PNO amplitudes into the untruncated virtual MO space. Therefore, we only demonstrate and benchmark the accuracy of the PNO-CEPT2 model for small- to medium-size molecules, and the assessing efficiency is beyond the scope of this manuscript.

D. PNO-based code generation

The automatic derivation and code generation technique has been a quite powerful strategy for developing and testing the novel wave function methods, which often involve hundreds or thousands of tensor contraction terms to implement.[91,97,98,108,111–130] To generate an efficient contraction code, each of the tensor contraction terms should be divided into a stream of binary contractions. This is also the case for the code generations employing the PNOs

spanning the virtual space. Even though the global optimization scheme proposed by Hanrath and Engels-Putzka for developing the efficient higher-order CC codes[131,132] can also be used in such a context, in order to keep the generator tool relatively simple yet effective, we use a more heuristic strategy for forming the optimal binary contractions.

In the canonical MO basis, typical contraction terms in the CEPT2 model read

$$\begin{aligned} r^{\rho}_{ab} \leftarrow & \frac{1}{4}\sum_{\tau}\sum_{pqrs}\sum_{c}(f_{\mathrm{core}})_{ca}D^{pq}_{rs}t^{\tau}_{cb}C^{\tau}_{sr}C^{\rho}_{pq} - \frac{1}{4}\sum_{\tau}\sum_{pqrst}(f_{\mathrm{core}})_{ts}D^{pq}_{rs}t^{\tau}_{ba}C^{\tau}_{pq}C^{\rho}_{tr} + \frac{1}{4}\sum_{\tau}\sum_{pqrstu}\sum_{c}(uc|qa)D^{pqr}_{stu}t^{\tau}_{cb}C^{\rho}_{st}C^{\tau}_{pr} \\ & + \frac{1}{4}\sum_{\tau}\sum_{pqrstuv}(ur|tv)D^{pqr}_{stu}t^{\tau}_{ba}C^{\rho}_{pq}C^{\tau}_{vs} - \frac{1}{4}\sum_{\tau}\sum_{pqrstu}(st|ru)D^{pq}_{rs}t^{\tau}_{ba}C^{\rho}_{qp}C^{\tau}_{ut} + \frac{1}{4}\sum_{\tau}\sum_{pqrs}\sum_{cd}(ac|bd)D^{pq}_{rs}t^{\tau}_{cd}C^{\rho}_{sr}C^{\tau}_{qp} \\ & + (18\ \text{more terms obtained by permuting pairs of indices}) \end{aligned} \tag{47}$$

for the $\{\Psi^{ab}_{\rho}\}$ subspace. Even though each term of Eq. (47) is composed of five tensor quantities resulting in 105 unique ways to form the binary contractions, we find that the RDM is always contracted with two orthonormalization matrices (**C**). Moreover, if the MO integral involves at least one active MO indices, it is also contracted either with an RDM or with one **C** matrix. Therefore, after forming such amplitude-independent intermediates, Eq. (47) becomes

$$\begin{aligned} r^{\rho}_{ab} \leftarrow & \frac{1}{4}\sum_{\tau}\sum_{c}(f_{\mathrm{core}})_{ca}(W_0)_{\rho\tau}t^{\tau}_{cb} - \frac{1}{4}\sum_{\tau}(fW_1)_{\rho\tau}t^{\tau}_{ba} \\ & + \frac{1}{4}\sum_{\tau}\sum_{c}(vW_2)_{\rho\tau,ca}t^{\tau}_{cb} + \frac{1}{4}\sum_{\tau}(W_3)_{\rho\tau}t^{\tau}_{ba} \\ & - \frac{1}{4}\sum_{\tau}\sum_{c}(W_4)_{\rho\tau}t^{\tau}_{ba} + \frac{1}{4}\sum_{\tau}\sum_{cd}(ac|bd)(W_5)_{\rho\tau}t^{\tau}_{cd} \\ & + (18\ \text{more terms obtained by permuting pairs of indices}). \end{aligned} \tag{48}$$

By comparing the indices of the amplitudes, the generator can form an additional intermediate

$$(xW_6)_{\rho\tau} = (fW_1)_{\rho\tau} + (W_4)_{\rho\tau} \tag{49}$$

and the number of amplitude-dependent contractions is further reduced. In our current PNO-CASPT2/CEPT2 implementation, all the amplitude-independent intermediates such as (W_n), (fW_n), (vW_n), and (xW_n) are constructed and stored in the fast core-memory before proceeding to the PCG iterations for solving the amplitude equations in the PNO space. The amplitude-independent intermediates are further subdivided into a stream of binary contractions and constructed using the DGEMM subroutine, assuming all the tensor quantities are stored in fast core-memory.

The CEPT2 residua [Eq. (48)] with an additional intermediate [Eq. (49)] are then transformed into the PNO-based computer code, assuming only the amplitudes and the residua are the native-PNO quantities. At each step of the PCG iterations, the amplitude-dependent intermediates involving a Fock matrix are constructed as

$$(fvvt)^{\rho}_{a_{\rho}b_{\rho}} = \sum_{c_{\rho}}(f_{\mathrm{core}})_{a_{\rho}c_{\rho}}t^{\rho}_{c_{\rho}b_{\rho}}, \tag{50}$$

$$(tfcc)^{\rho}_{a_{\rho i}b_{\rho i}} = \sum_{k}\sum_{a_{\rho k}b_{\rho k}}(f_{\mathrm{core}})_{ik}S_{a_{\rho i}a_{\rho k}}t^{\rho k}_{c_{\rho k}b_{\rho k}}S_{b_{\rho k}b_{\rho i}}, \tag{51}$$

where **S** represents the pair–pair overlap matrices that are all stored on the disk. As in the case of Eq. (48), if the pair indices of the amplitudes and the residuum, which are τ and ρ, respectively, are different, the generator calls a subroutine for projecting the amplitude from the τ-PNOs space to the ρ-PNO space. By this procedure, all the PNO-based tensor contractions that do not involve any two-electron integrals in Eq. (48) are transformed into

$$\begin{aligned} r^{\rho}_{a_{\rho}b_{\rho}} \leftarrow & \frac{1}{4}\sum_{\tau}(W_0)_{\rho\tau}\left[\sum_{a_{\tau}b_{\tau}}S_{a_{\rho}a_{\tau}}(fvvt)^{\tau}_{a_{\tau}b_{\tau}}S_{b_{\tau}b_{\rho}}\right] \\ & - \frac{1}{4}\sum_{\tau}(xW_6)_{\rho\tau}\left[\sum_{a_{\tau}b_{\tau}}S_{b_{\rho}b_{\tau}}t^{\tau}_{b_{\tau}a_{\tau}}S_{a_{\tau}a_{\rho}}\right] \\ & + \frac{1}{4}\sum_{\tau}(W_3)_{\rho\tau}\left[\sum_{a_{\tau}b_{\tau}}S_{b_{\rho}b_{\tau}}t^{\tau}_{ba}S_{a_{\tau}a_{\rho}}\right] \end{aligned} \tag{52}$$

and are constructed efficiently using DGEMM for projecting the PNOs from τ-pair to ρ-pair and DAXPY for summing up each contribution into the residua.

All the 4-external terms that appear in PNO-CEPT2, such as the sixth term in Eq. (48), have a similar structure to each other,

$$r^{\rho}_{a_{\rho}b_{\rho}} \leftarrow \frac{1}{4}\sum_{c_{\rho}d_{\rho}}(a_{\rho}c_{\rho}|b_{\rho}d_{\rho})\left[\sum_{\tau}(W_5)_{\rho\tau}\left[\sum_{c_{\tau}d_{\tau}}S_{a_{\rho}a_{\tau}}t^{\tau}_{c_{\tau}d_{\tau}}S_{b_{\tau}b_{\rho}}\right]\right], \tag{53}$$

$$r^{\rho i}_{a_{\rho i}b_{\rho i}} \leftarrow 2\sum_{c_{\rho i}d_{\rho i}}(a_{\rho i}c_{\rho i}|b_{\rho i}d_{\rho i})\left[\sum_{\tau}(W_{124})_{\rho\tau}\left[\sum_{c_{\tau i}d_{\tau i}}S_{a_{\rho i}a_{\tau i}}t^{\tau i}_{c_{\tau i}d_{\tau i}}S_{b_{\tau i}b_{\rho i}}\right]\right], \tag{54}$$

and so we have written an optimized subroutine for efficiently constructing those terms in the PNO basis, which are called by the generator. In Eqs. (53) and (54), the (W_n) intermediates are actually diagonal matrices and, hence, the 4-external terms take exactly the same form as those in the $r^{ij}_{a_{ij}b_{ij}}$ block of the PNO-CEPT2 residual. As we are not performing the pair-energy-based screening of ρi- and ρ-pairs, formal scaling for computing the 4-external terms [Eqs. (53) and (54)] is quadratic, assuming that the average number of PNOs per pair is asymptotically constant.

For those matrix blocks that do not involve any PNOs (A/A-blocks) and the coupling matrix elements of the canonical and the PNO subspaces (E/A- and A/E-blocks), the PNO-based amplitudes are back transformed into the canonical space and used to form the similar contractions.

III. RESULTS AND DISCUSSION

A. Non-parallelity errors for N_2 dissociation

To assess the performance of the canonical CEPT2 model and the validity of the PNO truncation, we calculated the dissociation curve of the N_2 molecule in the singlet state using the CEPT2 model with and without the PNO truncations in comparison with the FIC-NEVPT2 and CASPT2 results. The CEPT2 results are also compared with those obtained by higher-order approaches such as Davidson-corrected FIC-MRCI (MRCI+Q) and the Averaged-Coupled-Pair Functional (FIC-ACPF) and FIC-MR-CEPA/0. In all the CASPT2 and CEPT2 computations, no IPEA and level shifts were used. Errors from the FIC-MRCI+Q values are shown in Fig. 1. The non-parallelity errors (NPEs) are given in Table I. The Orca 4.2 program package[56] was used for FIC-NEVPT2, FIC-MRCI,[98] FIC-CEPA/0, and FIC-ACPF[133] computations. In Table I, NPE by the CEPT2 model is shown to be smaller than that of the CASPT2 by about 3.8 kcal/mol. Even though the NEVPT2 shows the largest deviations from the reference FIC-MRCI+Q results and the dynamical correlation energies recovered are smaller than those by CASPT2 by more than 15 kcal/mol, the NPE in the NEVPT2 energies is smaller than those by CASPT2 and CEPT2 models. The FIC-MRCI-based and its approximately size-consistent variants produce quite similar results, showing the NPE by up to about 2.0 kcal/mol with respect to the FIC-MRCI+Q results, even though their computational costs are higher than any of the CASPT2 and CEPT2 models.

In Table II, the dynamical correlation energies recovered by the PNO-CEPT2 model are shown for the N_2 molecule with various internuclear distances. To obtain approximately 99.9% of the correlation energy, the PNO truncation threshold, which is coined `TCutPNO`, should be tightened by up to 1.0×10^{-8}. Surprisingly, the correlation energy recovered appears to be smallest at 1.0 Å, which is close to the equilibrium internuclear distance where the static correlation effect is very minor in comparison with the dynamic counterpart. On the other hand, in the strongly correlated region where the triple bond is being broken, the PNO approximation performs relatively well recovering approximately 99.9% of the canonical correlation energy even with `TCutPNO` = 5.0×10^{-8}. The dynamical correlation energies calculated using a very loose

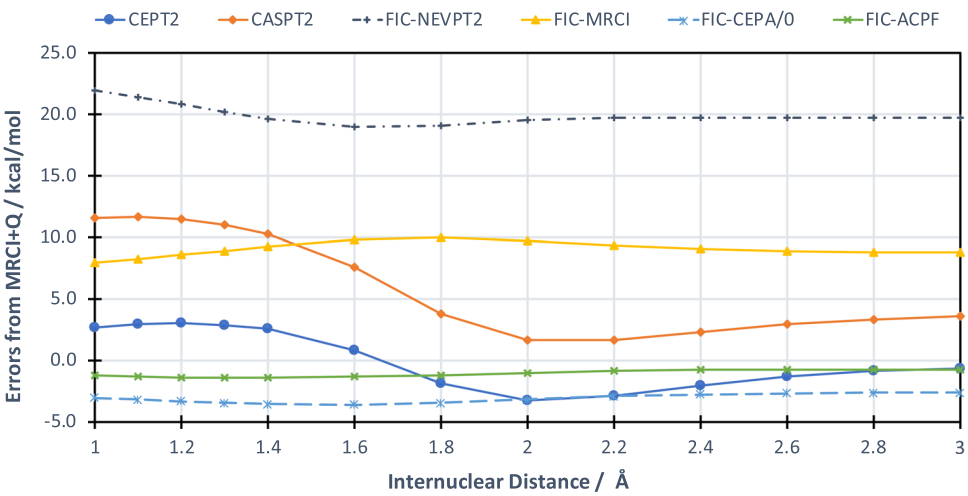

FIG. 1. Deviations of canonical CEPT2 energy from those of MRCI+Q for N_2 with various internuclear distances with the def2-QZVPP basis set. The 1*s* orbitals of nitrogen atoms were kept frozen, while all the other orbitals were correlated. All the 2*p* orbitals were included in the active space leading to CAS(6*e*, 6*o*) treatment.

TABLE I. The NPEs in kcal/mol for N_2 dissociation by various FIC methods with respect to the FIC-MRCI+Q energies.

	CASPT2	CEPT2	FIC-NEVPT2	FIC-MRCI	FIC-CEPA/0	FIC-ACPF
NPEs (kcal/mol)	9.98	6.21	2.99	2.03	0.98	0.68

TABLE II. Dynamic correlation energies recovered (%) by the PNO-CEPT2 model for N_2 with various PNO truncation thresholds with the def2-QZVPP[143,144] basis set. No pair-energy-based screening of weak-pairs was performed. The 1s orbitals of nitrogen atoms were kept frozen, while the 2*p* orbitals were included in the active space [CAS(6*e*, 6*o*)].

	TCutPNO										
R (N–N) (Å)	1.0×10^{-11}	1.0×10^{-10}	1.0×10^{-9}	5.0×10^{-9}	1.0×10^{-8}	5.0×10^{-8}	1.0×10^{-7}	5.0×10^{-7}	1.0×10^{-6}	5.0×10^{-6}	1.0×10^{-5}	1.0×10^{-4}
1.0	99.95	99.95	99.93	99.93	99.88	99.83	99.79	99.68	99.64	99.37	99.15	96.58
1.1	99.95	99.95	99.94	99.92	99.90	99.84	99.80	99.72	99.67	99.52	99.30	96.37
1.2	99.95	99.95	99.94	99.91	99.90	99.86	99.81	99.73	99.71	99.62	99.50	96.13
1.3	99.95	99.95	99.94	99.92	99.91	99.87	99.83	99.75	99.73	99.65	99.60	96.13
1.4	99.95	99.95	99.94	99.93	99.92	99.88	99.85	99.80	99.75	99.69	99.71	96.79
1.6	99.96	99.96	99.95	99.94	99.93	99.90	99.89	99.86	99.81	99.86	99.85	97.74
1.8	99.97	99.97	99.96	99.95	99.95	99.93	99.92	99.91	99.86	100.02	100.06	98.52
2.0	99.98	99.98	99.97	99.96	99.96	99.96	99.95	99.95	99.87	100.09	100.18	99.18
2.2	99.98	99.98	99.98	99.98	99.97	99.97	99.96	99.96	99.86	100.12	100.16	99.76
2.4	99.99	99.98	99.98	99.98	99.98	99.97	99.97	99.96	99.85	100.14	100.10	99.94
2.6	99.99	99.99	99.98	99.98	99.98	99.97	99.97	99.96	99.85	100.15	100.15	100.19
2.8	99.99	99.99	99.98	99.98	99.98	99.97	99.97	99.96	99.85	100.13	100.16	100.34
3.0	99.99	99.99	99.99	99.98	99.98	99.97	99.96	99.96	99.85	100.13	100.18	100.43

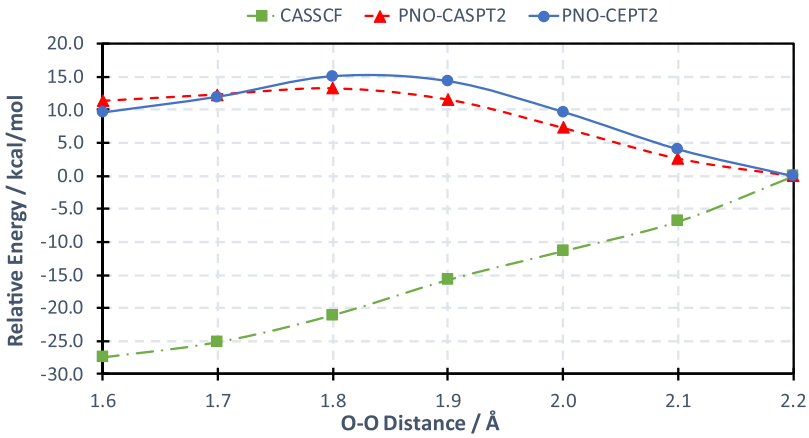

FIG. 2. Isomerization curves of $[Cu_2O_2]^{2+}(NH_3)_6$ calculated by PNO-CASPT2 and PNO-CEPT2 using def2-QZVPP (O, Cu) and def2-TZVPP (H, N) basis sets. For the RI treatment, the def2-TZVPP/C auxiliary basis was used. All the O(1*s*), N(1*s*), and Cu(1*s*, 2*s*, 2*p*) orbitals were kept frozen at the PNO-CASPT2/CEPT2 steps. The active space is composed of O($2p_x$, $2p_y$, $3p_x$, $3p_y$) and Cu($3d_{xy}$), thus leading to CAS(8*e*, 10*o*) treatment. The `TCutPNO` and `TCutPairs` thresholds were set to 5.0×10^{-8} and 1.0×10^{-5} Eh, respectively. Total number of AO basis functions is 752.

`TCutPNO` threshold often overshoot the canonical counterparts because the weak-pair and PNO truncation corrections become too large as reported, for instance, in Refs. 54 and 61.

B. Isomerization of $[Cu_2O_2]^{2+}(NH_3)_6$

We applied the PNO-CEPT2 model to the isomerization of the $[Cu_2O_2]^{2+}(NH_3)_6$ complex from the bis(μ-oxo) to the $\mu - \eta^2 : \eta^2$-peroxo structures, which is a typical benchmark system for MR methods.[108,134,135] The O_2 activation mechanism in enzymes such as hemocyanin is known to be mediated by interconversion of $[Cu_2(\mu - \eta^2 : \eta^2\text{-peroxo})]^{2+}$ and $[Cu_2(\mu\text{-oxo})]^{2+}$ cores. To accurately determine the isomerization pathways, numerous attempts have been made employing the $[Cu_2O_2]^{2+}(NH_3)_6$ complex as an active-site model for O_2 activation reactions.

A particular difficulty of the isomerization of this complex consists in the fact that the CASPT2 and MRCI+Q results strongly disagree with each other: With CAS(8*e*, 10*o*), the CASPT2 predicts that the bis(μ-oxo) structure is lower in the energy, while using the MRCI+Q and MR-ACPF models, the $\mu - \eta^2 : \eta^2$-peroxo structure appears to be more stable. Recently, Köhn and co-workers[108] performed a set of benchmark calculations on this system using IC-MR Coupled-Cluster (IC-MR-CC)[119,136] and the higher-order MRPT methods and found that all the higher-order methods than the second-order of perturbation expansion predict that the $\mu - \eta^2 : \eta^2$-peroxo structure is lower in energy. This is actually consistent with the partially IC-MRCI+Q calculations published by Rode and Werner.[134] To produce the consistent energy ordering to the partially IC-MRCI+Q and IC-MR-CC calculations using the CASPT2-type wave function, one has to employ a larger active space involving all the 3*d* and the double-shell 4*d* orbitals of copper atoms, thus leading to the active space composed of 24 electrons in 28 orbitals, as reported in the RAS(24*e*, 28*o*)PT2 study by Gagliardi and co-workers[11] and the cumulant-based DMRG-CASPT2 study by Yanai and co-workers.[135] Therefore, it is interesting to see how much improvement over the PNO-CASPT2 is obtained by the PNO-CEPT2 model while keeping the active space CAS(8*e*, 10*o*).

Isomerization energy profiles calculated by PNO-CASPT2/CEPT2 methods are shown in Fig. 2 as a function of O–O distance. The bis(μ-oxo) and $\mu - \eta^2 : \eta^2$-peroxo structures were taken from Ref. 91, and all the intermediate geometries were generated as a superposition of two isomeric geometries without performing any optimization. The isomerization energies [E($\mu - \eta^2 : \eta^2$-peroxo)-E(bis(μ-oxo))] calculated at CASSCF, PNO-CASPT2, and PNO-CEPT2 are −27.5 kcal/mol, +11.4 kcal/mol, and +9.6 kcal/mol, respectively, as given in Table III. The difference between the previous CASPT2(8*e*, 10*o*) results by Rode *et al.* and our PNO-CASPT2(8*e*, 10*o*) calculations with larger quadruple ζ basis sets

TABLE III. Isomerization energies calculated by the size-extensive version of the completely renormalized CCSD with perturbative triples (CR-CCSD(T)$_L$) and various MR methods. For the PNO-CASPT2/CEPT2 calculations, the PNO and weak-pair truncation thresholds were set to 5.0×10^{-8} and 1.0×10^{-5} Eh, respectively, and the relativistic effects were not included.

Method	E($\mu - \eta^2$:η^2-peroxo) −E(bis(μ-oxo)) (kcal/mol)
CR-CCSD(T)$_L$[a,b]	−10.1
FIC-MRCCSD(8*e*, 10*o*)[a,b]	−9.4
IC-MRCI+Q(8*e*, 10*o*)[a,b]	−12.4
DMRG-cu(4)-CASPT2(24*e*, 28*o*)[c]	−4.9
DMRG-CASSCF(24*e*, 28*o*)[c]	−21.3
RASPT2(24*e*, 28*o*)[b,d]	−7.6
CASSCF(16*e*, 14*o*)[a,b]	−29.8
CASPT2(16*e*, 14*o*)[a,b]	+17.2
CASSCF(8*e*, 10*o*)[b,e]	−23.4
CASPT2(8*e*, 10*o*)[b,e]	+10.2
IC-MRCI+Q(8*e*, 10*o*)[b,e]	−11.6
CASSCF(8*e*, 10*o*) (this work)	−27.5
PNO-CASPT2(8*e*, 10*o*) (this work)	+11.4
PNO-CEPT2(8*e*, 10*o*) (this work)	+9.6

[a] Taken from Ref. 108.
[b] Relativistic effects were included by the effective core potentials (ECPs) on copper atoms.
[c] Taken from Ref. 135.
[d] Taken from Ref. 11.
[e] Taken from Ref. 134.

stems from the difference in the basis sets and PNO and weak-pair truncation errors. Still, the difference reaches only up to about 1.2 kcal/mol and is quite small in comparison with a discrepancy between the MRCI+Q(8*e*, 10*o*) and CASPT2(8*e*, 10*o*) results. The PNO-CEPA extension in the PNO-CEPT2 model corrects the PNO-CASPT2 results in the direction of MRCI+Q(8*e*, 10*o*) result by up to about 1.8 kcal/mol. In Table IV, the magnitude of the PNO-CEPT2 corrections to each subspace is analyzed. As can be seen, the CEPA extension to the $(c, c) \rightarrow (v, v)$ subspace corrects the dynamical correlation energy by about up to −21.0 kcal/mol for both bis(μ-oxo) and $\mu - \eta^2 : \eta^2$-peroxo states, thus resulting in almost perfect cancellation in the isomerization energy. The 2-external subspaces with at least one active MO indices give rise to a larger change in isomerization energy by up to 1.52 kcal/mol. Even though the zeroth-order Hamiltonian is left unmodified, the $(c, c) \rightarrow (a, v)$ semi-internal subspace shows a relatively large correction of about 0.45 kcal/mol in comparison with that from the other semi-internal and internal subspaces. However, the isomerization energy profile calculated by the PNO-CEPT2 model is still close enough to that by PNO-CASPT2, and the isomerization energy still appears to be far off from the partially IC-MRCI+Q and IC-MR-CC values. Therefore, at least in this case, the CEPA extension in the 2-external subspaces gives only a minor correction to the CASPT2 isomerization energy.

C. Ground and excited states of butadiene and linear polyenes

Predicting low-lying dark ($2^1A_g^-$) and bright ($1^1B_u^+$) excited states of butadiene has been known as notoriously challenging despite as reported in Ref. 137. To achieve qualitative accuracy in calculating the EE for the accessible $1^1B_u^+$ state, inclusion of the dynamic correlation plays a key role. On the other hand, the dipole-forbidden $2^1A_g^-$ state is dominated by doubly excited character and is of strong MR nature even though there is no reliable experimental EEs reported for this state. Therefore, the typical SR excited state methods such as Equation-Of-Motion Coupled-Cluster with Singles and Doubles (EOM-CCSD) are not of appropriate choices for the $2^1A_g^-$ state.

In Table V, EEs for the $1^1B_u^+$ and $2^1A_g^-$ states calculated by the canonical CASPT2 and CEPT2 models for butadiene are shown in comparison with various theoretical and experimental values. The reference CASSCF wave functions were calculated in a state specific (SS) manner to each of $1^1A_g^-$, $2^1A_g^-$ and $1^1B_u^+$ states. Geometries for butadiene and longer polyene chains were taken from Ref. 135. In Ref. 137, Watson and Chan have proposed the best theoretical EEs by using the EOM-CC method including up to quadruple excitations (EOM-CCSDTQ). It is seen that the CC2, EOM-CCSD, and EOM-CCSD(T) values largely deviate from the EOM-CCSDTQ values for the $2^1A_g^-$ state that possesses doubly excited character while giving reasonably well agreement for the $1^1B_u^+$ state. To obtain a good agreement with the EOM-CCSDTQ results for both states in a SR framework, at least, the CC3 level of theory should be used. The CASSCF values, which lack dynamic correlation effects, show a large deviation by up to 2.3 eV from the EOM-CCSDTQ result for the $1^1B_u^+$ state. Addition of the dynamic correlation correction on top of the CASSCF energies significantly remedies the CASSCF results, and the CASPT2 gives reasonably well agreement with the EOM-CCSDTQ values, while in the CASPT2 results in Ref. 138, $1^1B_u^+$ and $2^1A_g^-$ are predicted to be almost degenerated. The EEs calculated by the CEPT2 model are quite close to those by MR-AQCC results and in good agreement with the EOM-CCSDTQ results.

TABLE IV. Contributions from each subspace in the PNO-CASPT2 and PNO-CEPT2 dynamical correlation energies using TCutPairs = 1.0×10^{-5} Eh and TCutPNO = 5.0×10^{-8} for the $[Cu_2O_2]^{2+}(NH_3)_6$ complex. Magnitude of PNO-CEPT2 correction (δE_{CEPA}) in each subspace is compared with that of PNO-CASPT2. In addition, difference between PNO-CEPT2 corrections for two geometries, $\delta E_{CEPA}(R_{O-O} = 1.6$ Å)–$\delta E_{CEPA}(R_{O-O} = 2.2$ Å), are also shown as Δ-correction.

	$R_{O-O} = 1.6$ Å			$R_{O-O} = 2.2$ Å			
Subspace	PNO-CASPT2 (Eh)	PNO-CEPT2 (Eh)	δE_{CEPA} (kcal/mol)	CASPT2 (Eh)	CEPT2 (Eh)	δE_{CEPA} (kcal/mol)	Δ-correction (kcal/mol)
External							
$(c, c) \rightarrow (v, v)$	−2.641 691	−2.675 058	(−20.94)	−2.632 592	−2.666 005	(−20.97)	(0.03)
$(c, a) \rightarrow (v, v)$	−0.320 316	−0.303 014	(10.86)	−0.331 461	−0.312 859	(11.67)	(−0.82)
$(a, a) \rightarrow (v, v)$	−0.051 163	−0.052 895	(−1.09)	−0.053 697	−0.054 310	(−0.39)	(−0.70)
Sum							(−1.49)
Semi-internal							
$(c, c) \rightarrow (a, v)$	−0.132 298	−0.130 746	(0.97)	−0.154 270	−0.152 005	(1.42)	(−0.45)
$(c, a) \rightarrow (a, v), (c, a) \rightarrow (v, a)$	−0.206 663	−0.207 394	(−0.46)	−0.238 979	−0.239 850	(−0.55)	(0.09)
$(a, a) \rightarrow (a, v)$	−0.015 565	−0.015 542	(0.01)	−0.013 961	−0.013 962	(0.00)	(0.02)
Sum							(−0.34)
Internal							
$(c, c) \rightarrow (a, a)$	−0.006 854	−0.006 793	(0.04)	−0.009 053	−0.008 963	(0.06)	(−0.02)
$(c, a) \rightarrow (a, a)$	−0.006 606	−0.006 607	(0.00)	−0.009 019	−0.009 018	(0.00)	(0.00)
Sum							(−0.02)
Total sum							(−1.85)

TABLE V. Computed EEs for $1^1B_u^+$ and $2^1A_g^-$ states of the butadiene molecule at the canonical CASPT2 and CEPT2 model in comparison with various theoretical and experimental data. The def2-TZVPP basis and def2-TZVPP/JK auxiliary basis sets were used. The C(1*s*) orbitals were frozen during CASPT2 and CEPT2 computations, while all the C($2p_z$) orbitals were included in the active space leading to CAS(4*e*, 4*o*) treatment. No shifts were used in the zeroth-order Hamiltonian.

Method	$1^1B_u^+$	$2^1A_g^-$
EOM-CCSD[145]	6.42	7.23
EOM-CCSD(T)[145]	6.13–6.36	6.76–6.92
CC2[146]	6.15	7.04
CC3[146]	6.19	6.58
CASSCF[138]	8.54	6.64
CASPT2[138]	6.23	6.27
MRCI[147]	6.70	6.78
MR-AQCC[148]	6.18	6.55
SS-CASSCF (this work)	8.18	6.72
CASPT2 (this work)	6.00	6.29
CEPT2 (this work)	6.12	6.50
EOM-CCSDTQ[137]	6.21	6.41
Expt.[149]	5.96–6.05	...

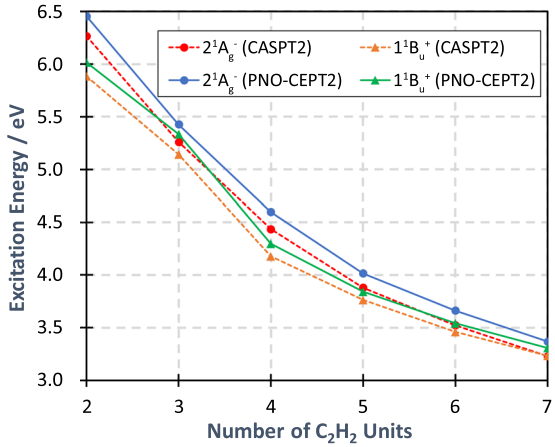

FIG. 3. Vertical EEs for linear polyene, $C_{2n}H_{2n+2}$, where n = 2–7, calculated by canonical CASPT2 and the PNO-CEPT2 methods. For the PNO-CEPT2 computation, PNO and weak-pair truncation thresholds were set to 5.0×10^{-8} Eh and 1.0×10^{-5} Eh, respectively. The def2-TZVPP basis and def2-TZVPP/JK auxiliary basis sets were used. All the C(1*s*) orbitals were kept frozen after the reference CASSCF calculation, while C($2p_z$) orbitals were included in the active space, thus leading to CAS(2n *e*, 2n *o*) treatment. No shifts were used in the zeroth-order Hamiltonian.

The $1^1B_u^+$ and $2^1A_g^-$ states of longer polyene chains were used as a benchmark set for the cumulant-approximated CASPT2[135] and NEVPT2[139] studies to assess the errors caused by the cumulant approximations in the 3- and 4-RDMs. In this study, we do not utilize the cumulant approximations in the RDMs. To assess the impact of CEPA/0 extensions in the PNO-CEPT2 model, we calculated the vertical EEs for $1^1B_u^+$ and $2^1A_g^-$ states of the conjugated linear polyene molecules ($C_{2n}H_{2n+2}$) using CAS(2n*e*, 2n*o*). As SS-CASSCF calculations did not converge to C_6H_8 and longer polyenes, we performed state-averaged (SA-) CASSCF calculations involving three lowest A_g and B_u states for obtaining the MOs for the $^1A_g^-$ and $1^1B_u^+$ states, respectively. The following CASPT2 and PNO-CEPT2 computations were performed in a SS manner to each state.

In Fig. 3, the EEs calculated at the canonical CASPT2 and PNO-CEPT2 levels are shown. As shown in Fig. 3, the EEs calculated by the PNO-CEPT2 model are always higher than those by the CASPT2 theory. This means that the PNO-CEPA/0 correction on the ground $1^1A_g^-$ state is even larger than on the $1^1B_u^+$ and $2^1A_g^-$ states.

The doubly excited $2^1A_g^-$ state is higher in energy than the bright $1^1B_u^+$ state by 0.06 eV for $C_{14}H_{16}$, and the crossover is not observed at the PNO-CEPT2 level in Fig. 3. On the other hand, at the CASPT2 level, the $2^1A_g^-$ is calculated to be very slightly lower in the energy for $C_{14}H_{16}$ by up to 0.002 eV. By treating the external IC configurations at the CEPA/0 level in the PNO-CEPT2 model for recovering a more dynamic correlation effect, the valence $1^1B_u^+$ state is more lowered in the energy than the doubly excited $2^1A_g^-$ state. This behavior of the CASPT2 model is actually in contrast to previous studies such as Ref. 135 where the $2^1A_g^-$ state becomes lower in the energy for C_8H_{10} with the cc-pVDZ basis set. We found that the use of a larger def2-TZVPP basis set drastically stabilizes the $1^1B_u^+$ state relatively largely influenced by dynamic correlation effects in comparison with the $2^1A_g^-$ state of strong MR character, thus pushing the crossover point to even longer polyenes. Moreover, the $1^1B_u^+$ and higher $^1B_u^-$ states are closely lying in the energy at the CASSCF level for C_6H_8, thus showing a discontinuity. For a more thorough computation of the quasi-degenerated electronic states at the PNO-CEPT level, multi-state (MS)[140] or the extended multi-state (XMS)[141] extension is necessary.

D. Singlet-triplet gap of free-base porphyrin

We calculated the non-vertical singlet–triplet (S–T) energy gaps of a free-base porphyrin molecule. The geometries for S_0 and T_0 states of free-base porphyrin were taken from Ref. 95. In Table VI, the S–T gaps and the dynamic correlation energies recovered by various PNO cutoff thresholds are shown. It is seen that the PNO-CASPT2 model shows good agreement with the experimental value for all the PNO truncation thresholds even for quite loose threshold such as 1.0×10^{-6}, thus indicating that the error cancellation works surprisingly fine for this systems. This is most probably due to the fact that the S_0 and T_0 geometries are similar enough to each other. The PNO-CEPT2 model gives even closer values to the experimental one. The compression ratios of the first-order amplitudes, which are calculated as a ratio between the total number of amplitudes in Eq. (19) and the canonical counterpart, are also shown. Even with the tightest threshold used, 1.0×10^{-9}, the PNO-CASPT2/CEPT2 models require only less than 6% of the amplitudes while giving quite good agreement with the untruncated value. The PNO-CEPT2 values also agree well to the cumulant-approximated MRCI+Q and ACPF results that use the DMRG-CASSCF reference function with a full-valence π active space. Note that none of the computational values in Table VI include the solvent-effects.

TABLE VI. Dynamic electron correlation energies and S–T gaps for free-base porphyrin calculated at the PNO-CASPT2/CEPT2 level with various PNO cutoff thresholds in comparison with the experimental S–T gap. The def2-SVP basis set was used. The threshold for weak-pair screening was set to 1×10^{-5} Eh. All the 1*s* orbitals of carbon atoms were kept frozen. 8π MOs composed of 2p_z orbitals of carbon atoms were included in the active space, thus leading to CAS(8*e*, 8*o*) settings, which is consistent with CAS treatment of Ref. 150. Ratios between the total number of PNO-CASPT2/CEPT2 amplitudes to optimize and that of canonical CASPT2, both of which include internal and semi-internal amplitudes, are also shown. Total number of AO basis functions is 406.

TCutPNO	Total energy (S_0) (Eh)	Correlation energy (Eh)	Accuracy (%)	Compression ratio (%)	Total energy (T_0) (Eh)	Correlation energy (Eh)	Accuracy (%)	Compression ratio (%)	S–T gap (eV)
				PNO-CASPT2					
Full	−985.795 110	−3.233 234	(100.00)	(100.00)	−985.733 659	−3.219 267	(100.00)	(100.00)	1.67
1.0×10^{-9}	−985.791 357	−3.229 481	(99.88)	(5.83)	−985.729 366	−3.214 973	(99.87)	(4.69)	1.69
1.0×10^{-8}	−985.790 258	−3.228 382	(99.85)	(3.02)	−985.728 332	−3.213 940	(99.83)	(2.56)	1.69
5.0×10^{-8}	−985.788 902	−3.227 025	(99.81)	(1.90)	−985.726 937	−3.212 544	(99.79)	(1.68)	1.69
1.0×10^{-7}	−985.787 947	−3.226 070	(99.78)	(1.57)	−985.725 979	−3.211 586	(99.76)	(1.41)	1.69
1.0×10^{-6}	−985.781 456	−3.219 580	(99.58)	(0.94)	−985.719 703	−3.205 310	(99.57)	(0.90)	1.68
				PNO-CEPT2					
1.0×10^{-9}	−985.982 732	−3.420 855	...	(5.83)	−985.925 605	−3.411 212	...	(4.69)	1.55
1.0×10^{-8}	−985.981 451	−3.419 574	...	(3.02)	−985.924 399	−3.410 006	...	(2.56)	1.55
5.0×10^{-8}	−985.979 903	−3.418 026	...	(1.90)	−985.922 854	−3.408 461	...	(1.68)	1.55
1.0×10^{-7}	−985.978 852	−3.416 975	...	(1.57)	−985.921 792	−3.407 399	...	(1.41)	1.55
1.0×10^{-6}	−985.973 026	−3.411 150	...	(0.94)	−985.916 193	−3.401 800	...	(0.90)	1.55
				Other methods					
DMRG-CASSCF(26*e*, 24*o*)[95]									1.26
DMRG-cu(4)-MRCI(26*e*, 24*o*)[95]									1.41
DMRG-cu(4)-MRCI+Q(26*e*, 24*o*)[95]									1.48
DMRG-cu(4)-ACPF(26*e*, 24*o*)[95]									1.55
Diffusion Monte Carlo (DMC)[151]									1.60
Expt.[152]									1.58

TABLE VII. Contribution from each subspace in the PNO-CASPT2 and PNO-CEPT2 dynamical correlation energies using TCutPairs = 1.0×10^{-5} Eh and TCutPNO = 5.0×10^{-8} for free-base porphyrin in singlet and triplet states. Magnitude of PNO-CEPT2 correction (δE_{CEPA}) in each subspace is compared with that of PNO-CASPT2. In addition, difference between PNO-CEPT2 corrections for two geometries, $\delta E_{CEPA}(T_0)$-$\delta E_{CEPA}(S_0)$), are also shown as Δ-correction.

	S_0 state			T_0 state			
Subspace	PNO-CASPT2 (Eh)	PNO-CEPT2 (Eh)	δE_{CEPA} (kcal/mol)	CASPT2 (Eh)	CEPT2 (Eh)	δE_{CEPA} (kcal/mol)	Δ-correction (kcal/mol)
External							
$(c, c) \rightarrow (v, v)$	−2.380 046	−2.571 048	(−119.86)	−2.416 554	−2.612 158	(−122.74)	(−2.89)
$(c, a) \rightarrow (v, v)$	−0.401 660	−0.401 882	(−0.14)	−0.377 783	−0.377 975	(−0.12)	(0.02)
$(a, a) \rightarrow (v, v)$	−0.027 777	−0.027 339	(0.27)	−0.022 754	−0.022 585	(0.11)	(−0.17)
Sum							(−3.04)
Semi-internal							
$(c, c) \rightarrow (a, v)$	−0.223 743	−0.223 854	(−0.07)	−0.208 821	−0.209 014	(−0.12)	(−0.05)
$(c, a) \rightarrow (a, v)$, $(c, a) \rightarrow (v, a)$	−0.166 721	−0.166 812	(−0.06)	−0.155 565	−0.155 614	(−0.03)	(0.03)
$(a, a) \rightarrow (a, v)$	−0.008 111	−0.008 122	(−0.01)	−0.012 407	−0.012 445	(−0.02)	(−0.02)
Sum							(−0.04)
Internal							
$(c, c) \rightarrow (a, a)$	−0.014 448	−0.014 450	(0.00)	−0.009 582	−0.009 587	(0.00)	(0.00)
$(c, a) \rightarrow (a, a)$	−0.004 442	−0.004 442	(0.00)	−0.009 023	−0.009 026	(0.00)	(0.00)
Sum							(0.00)
Total sum							(−3.08)

In Table VII, dynamic correlation contribution from each subspace is shown for both PNO-CASPT2 and PNO-CEPT2 models. Interestingly, unlike the isomerization of the $[Cu_2O_2]^{2+}(NH_3)_6$ complex, the $(c, c) \rightarrow (v, v)$ subspace, treated as a CEPA level, which does not involve any active MO indices, gives dominant correction to the S–T gap by up to −2.98 kcal/mol (−0.15 eV). On the other hand, the other two types of external subspaces give quite minor corrections that reach only to −0.15 kcal/mol in total.

IV. CONCLUSION

To obtain quantitative accuracy in predicting the reaction energies and various chemical energetics, a balanced treatment between static and dynamic electron correlation effects plays a key role. One of the most commonly used methods is the MR second-order perturbation theory such as CASPT2 and NEVPT2, both of which converge to the MP2 method in the closed-shell SR limit. As a simple yet higher order extension to the CASPT2 method, we have developed a hybrid of MR-CEPA/0 and CASPT2 *Ansätze* that converges to the CEPA/0(D) in the closed-shell SR limit, which is coined CEPT2 *Ansatz*. One of the largest bottlenecks of the CEPT2 computation that stems from the MR-CEPA/0 terms in the residual equations is the presence of the so-called 4-EEOs involving a contraction of the 4-external two-electron integrals and the amplitude. To accelerate the CEPT2 computation, the CEPT2 equations are expanded in the local PNO basis, which is a compact set of virtual orbitals specifically optimized to each pair of localized orbitals and the nr-ICB functions. Development of the PNO-CEPT2 computer programs was conducted using the automatic code generation technique and interfaced to our in-house quantum chemistry program package.

For N_2 dissociation, the CEPT2 model was shown to give a smaller NPE than that of the CASPT2 model in comparison with the reference FIC-MRCI+Q results. The errors caused by the PNO truncation were examined and shown to be the largest at around the equilibrium internuclear distance.

The PNO-CEPT2 model was applied to calculate the isomerization energy profiles of the $[Cu_2O_2]^{2+}(NH_3)_6$ complex from the bis(μ-oxo) to $\mu - \eta^2 : \eta^2$-peroxo structures. The PNO-CEPT2 results show a similar trend to the CASPT2 as long as CAS(8*e*, 10*o*) is used and strongly disagree with the previous partial IC-MRCI+Q and IC-MR-CC results. To remedy the accuracy of the PNO-CEPT2 model, the higher-order treatment of the subspaces with three active MO indices (E^{ip}_{qr} and E^{ra}_{pq}) will be necessary. However, a simple use of the IC-MR-CEPA *Ansatz* into those subspaces introduces a complicated tensor contraction involving the 4-RDMs and the amplitude. Moreover, the use of the PNOs cannot accelerate the construction of such terms. Another possibility to improve the accuracy of the PNO-CEPT2 model is to use an unconventionally large active space using the DMRG reference function.[5,135,142] As all the terms involving the 4-RDMs are not more complicated than those in the CASPT2 model, combination of the PNO-CEPT2 model and the DMRG reference function via the use of the cumulant-approximated 4-RDM[135] is quite straightforward. Nevertheless, previous studies have shown that a simple use of cumulant-approximated RDM often introduces unavoidable instability in the residual equation.[139] Therefore, as a future development, we prefer to pursue other possibilities such as decontracting the internal E^{ip}_{qr} and semi-internal E^{ra}_{pq} subspaces using the Matrix-Product State (MPS) basis.

The CEPT2 was shown to give good agreement with the EOM-CCSDTQ results on calculating the excitation energies of butadiene achieving a good balance between dynamic and static electron correlations. For longer polyene systems, the PNO-CEPT2 produces the larger EEs than those by the CASPT2 model by up to 0.29 eV.

For calculating the non-vertical S–T gap of free-base porphyrin where the relaxation of the geometry in the triplet state is relatively small, the PNO and weak-pair truncations work surprisingly fine, thus producing a S–T gap in good agreement with the experimental value. The size of the PNO-CEPT2 amplitudes is only up to less than 6% of the canonical counterpart even with the PNO and the weak-pair truncation thresholds set to 1.0×10^{-9} and 1.0×10^{-5} Eh, respectively.

It has been found that our CEPT2 model that is derived by embedding the high-level CEPA based 2-external corrections into the CASPT2 model leads to a solid improvement in the accuracy. However, when CASPT2 performs poorly for describing the semi-internal and internal components, the CEPT2 that inherits the CASPT2 for these subspaces can give poor results. This was observed to occur particularly when the active space or zeroth-order treatment was insufficient. To improve the accuracy without enlarging the active space, the higher order extension to the internal E^{ip}_{qr} and semi-internal E^{ra}_{pq} subspaces should be considered as an important topic of research. A production level implementation of the PNO-CEPT2 model is currently in progress.

SUPPLEMENTARY MATERIAL

See the supplementary material for actual formulas for the zeroth-order Hamiltonian and the overlap matrix elements over the redundant ICB functions, the orthonormalized and back-orthonormalized amplitudes, the total electronic energies for the dissociation of N_2, isomerization of the $[Cu_2O_2]^{2+}(NH_3)_6$ complex, and the low-lying electronic states of polyenes.

ACKNOWLEDGMENTS

T.Y. was supported by JST, PRESTO (Grant No. 17937609).

REFERENCES

[1] F. Neese, Coord. Chem. Rev. **253**, 526 (2009), theory and computing in contemporary coordination chemistry.
[2] D. I. Lyakh, M. Musiał, V. F. Lotrich, and R. J. Bartlett, Chem. Rev. **112**, 182 (2012).
[3] P. G. Szalay, T. Müller, G. Gidofalvi, H. Lischka, and R. Shepard, Chem. Rev. **112**, 108 (2012).
[4] J. P. Malrieu, R. Caballol, C. J. Calzado, C. de Graaf, and N. Guihéry, Chem. Rev. **114**, 429 (2014).
[5] E. Neuscamman, T. Yanai, and G. K.-L. Chan, Int. Rev. Phys. Chem. **29**, 231 (2010).
[6] B. O. Roos, P. R. Taylor, and P. E. Siegbahn, Chem. Phys. **48**, 157 (1980).
[7] B. O. Roos, Adv. Chem. Phys. **69**, 399 (1987).
[8] K. Ruedenberg, L. M. Cheung, and S. T. Elbert, Int. J. Quantum Chem. **16**, 1069 (1979).
[9] K. Kowalski and P. Piecuch, J. Chem. Phys. **113**, 18 (2000).
[10] K. Kowalski and P. Piecuch, J. Chem. Phys. **113**, 5644 (2000).

[11]C. J. Cramer, M. Włoch, P. Piecuch, C. Puzzarini, and L. Gagliardi, J. Phys. Chem. A **110**, 1991 (2006).
[12]J. J. Eriksen and J. Gauss, J. Chem. Theory Comput. **15**, 4873 (2019).
[13]Y. Qiu, T. M. Henderson, J. Zhao, and G. E. Scuseria, J. Chem. Phys. **147**, 064111 (2017).
[14]Y. Qiu, T. M. Henderson, J. Zhao, and G. E. Scuseria, J. Chem. Phys. **149**, 164108 (2018).
[15]J. A. Gomez, T. M. Henderson, and G. E. Scuseria, J. Chem. Phys. **150**, 144108 (2019).
[16]T. Tsuchimochi and S. Ten-no, J. Chem. Theory Comput. **12**, 1741 (2016).
[17]T. Tsuchimochi and S. L. Ten-no, J. Chem. Phys. **149**, 044109 (2018).
[18]E. Xu and S. L. Ten-no, J. Comput. Chem. **39**, 875 (2018).
[19]K. Andersson, P. A. Malmqvist, B. O. Roos, A. J. Sadlej, and K. Wolinski, J. Phys. Chem. **94**, 5483 (1990).
[20]K. Andersson, P. Malmqvist, and B. O. Roos, J. Chem. Phys. **96**, 1218 (1992).
[21]M. Schreiber, M. R. Silva-Junior, S. P. A. Sauer, and W. Thiel, J. Chem. Phys. **128**, 134110 (2008).
[22]S. Vancoillie, H. Zhao, M. Radoń, and K. Pierloot, J. Chem. Theory Comput. **6**, 576 (2010).
[23]Q. M. Phung and K. Pierloot, J. Chem. Theory Comput. **15**, 3033 (2019).
[24]P.-Å. Malmqvist, K. Pierloot, A. Rehaman, M. Shahi, C. J. Cramer, and L. Gagliardi, J. Chem. Phys. **128**, 204109 (2008).
[25]Q. M. Phung and K. Pierloot, Chem. - Eur. J. **25**, 12491 (2019).
[26]B. O. Roos and K. Andersson, Chem. Phys. Lett. **245**, 215 (1995).
[27]N. Forsberg and P.-Å. Malmqvist, Chem. Phys. Lett. **274**, 196 (1997).
[28]C. Angeli, R. Cimiraglia, S. Evangelisti, T. Leininger, and J. P. Malrieu, J. Chem. Phys. **114**, 10252 (2001).
[29]C. Angeli, R. Cimiraglia, and J. Malrieu, J. Chem. Phys. **117**, 9138 (2002).
[30]C. Angeli, M. Pastore, and R. Cimiraglia, Theor. Chem. Acc. **117**, 743 (2006).
[31]K. G. Dyall, J. Chem. Phys. **102**, 4909 (1995).
[32]C. Møller and M. S. Plesset, Phys. Rev. **46**, 618 (1934).
[33]F. Aquilante, T. K. Todorova, L. Gagliardi, T. B. Pedersen, and B. O. Roos, J. Chem. Phys. **131**, 034113 (2009).
[34]J. Segarra-Martí, M. Garavelli, and F. Aquilante, J. Chem. Theory Comput. **11**, 3772 (2015).
[35]F. Aquilante, T. B. Pedersen, R. Lindh, B. O. Roos, A. Sánchez de Merás, and H. Koch, J. Chem. Phys. **129**, 024113 (2008).
[36]J. Boström, F. Aquilante, T. B. Pedersen, and R. Lindh, J. Chem. Theory Comput. **5**, 1545 (2009).
[37]F. Aquilante, P.-Å. Malmqvist, T. B. Pedersen, A. Ghosh, and B. O. Roos, J. Chem. Theory Comput. **4**, 694 (2008).
[38]J. Boström, M. G. Delcey, F. Aquilante, L. Serrano-Andrés, T. B. Pedersen, and R. Lindh, J. Chem. Theory Comput. **6**, 747 (2010).
[39]C. Song and T. J. Martínez, J. Chem. Phys. **149**, 044108 (2018).
[40]W. Győffy, T. Shiozaki, G. Knizia, and H.-J. Werner, J. Chem. Phys. **138**, 104104 (2013).
[41]F. Menezes, D. Kats, and H.-J. Werner, J. Chem. Phys. **145**, 124115 (2016).
[42]D. Kats and H.-J. Werner, J. Chem. Phys. **150**, 214107 (2019).
[43]W. Kutzelnigg, J. Chem. Phys. **40**, 3640 (1964).
[44]R. Ahlrichs and W. Kutzelnigg, J. Chem. Phys. **48**, 1819 (1968).
[45]C. Edmiston and M. Krauss, J. Chem. Phys. **42**, 1119 (1965).
[46]C. Edmiston and M. Krauss, J. Chem. Phys. **45**, 1833 (1966).
[47]W. Meyer, Int. J. Quantum Chem. **5**, 341 (1971).
[48]W. Meyer, J. Chem. Phys. **58**, 1017 (1973).
[49]R. Ahlrichs and W. Kutzelnigg, Theor. Chim. Acta **10**, 377 (1968).
[50]P. R. Taylor, J. Chem. Phys. **74**, 1256 (1981).
[51]R. Fink and V. Staemmler, Theor. Chim. Acta **87**, 129 (1993).
[52]F. Neese, F. Wennmohs, and A. Hansen, J. Chem. Phys. **130**, 114108 (2009).
[53]F. Neese, A. Hansen, and D. G. Liakos, J. Chem. Phys. **131**, 064103 (2009).
[54]A. Hansen, D. G. Liakos, and F. Neese, J. Chem. Phys. **135**, 214102 (2011).
[55]D. G. Liakos, A. Hansen, and F. Neese, J. Chem. Theory Comput. **7**, 76 (2011).
[56]F. Neese, Wiley Interdiscip. Rev.: Comput. Mol. Sci. **8**, e1327 (2018).
[57]C. Riplinger and F. Neese, J. Chem. Phys. **138**, 034106 (2013).
[58]C. Riplinger, B. Sandhoefer, A. Hansen, and F. Neese, J. Chem. Phys. **139**, 134101 (2013).
[59]P. Pinski, C. Riplinger, E. F. Valeev, and F. Neese, J. Chem. Phys. **143**, 034108 (2015).
[60]C. Riplinger, P. Pinski, U. Becker, E. F. Valeev, and F. Neese, J. Chem. Phys. **144**, 024109 (2016).
[61]M. Saitow, U. Becker, C. Riplinger, E. F. Valeev, and F. Neese, J. Chem. Phys. **146**, 164105 (2017).
[62]D. Datta, S. Kossmann, and F. Neese, J. Chem. Phys. **145**, 114101 (2016).
[63]O. Demel, J. Pittner, and F. Neese, J. Chem. Theory Comput. **11**, 3104 (2015).
[64]J. Brabec, J. Lang, M. Saitow, J. Pittner, F. Neese, and O. Demel, J. Chem. Theory Comput. **14**, 1370 (2018).
[65]J. Lang, J. Brabec, M. Saitow, J. Pittner, F. Neese, and O. Demel, Phys. Chem. Chem. Phys. **21**, 5022 (2019).
[66]Y. Guo, K. Sivalingam, E. F. Valeev, and F. Neese, J. Chem. Phys. **144**, 094111 (2016).
[67]H.-J. Werner, G. Knizia, C. Krause, M. Schwilk, and M. Dornbach, J. Chem. Theory Comput. **11**, 484 (2015).
[68]M. Schwilk, D. Usvyat, and H.-J. Werner, J. Chem. Phys. **142**, 121102 (2015).
[69]M. Schwilk, Q. Ma, C. Köppl, and H.-J. Werner, J. Chem. Theory Comput. **13**, 3650 (2017).
[70]H. J. Werner, J. Chem. Phys. **145**, 201101 (2016).
[71]Q. Ma and H. J. Werner, J. Chem. Theory Comput. **14**, 198–215 (2018).
[72]C. Krause and H.-J. Werner, J. Chem. Theory Comput. **15**, 987 (2018).
[73]Q. Ma and H.-J. Werner, J. Chem. Theory Comput. **15**, 1044 (2019).
[74]G. Schmitz, B. Helmich, and C. Hättig, Mol. Phys. **111**, 2463 (2013).
[75]M. S. Frank, G. Schmitz, and C. Hättig, Mol. Phys. **115**, 343 (2017).
[76]G. Schmitz and C. Hättig, J. Chem. Phys. **145**, 234107 (2016).
[77]D. P. Tew and C. Hättig, Int. J. Quantum Chem. **113**, 224 (2013).
[78]G. Schmitz, C. Hättig, and D. P. Tew, Phys. Chem. Chem. Phys. **16**, 22167 (2014).
[79]D. P. Tew, B. Helmich, and C. Hättig, J. Chem. Phys. **135**, 074107 (2011).
[80]B. Helmich and C. Hättig, J. Chem. Phys. **135**, 214106 (2011).
[81]C. Hättig, D. P. Tew, and B. Helmich, J. Chem. Phys. **136**, 204105 (2012).
[82]B. Helmich and C. Hättig, J. Chem. Phys. **139**, 084114 (2013).
[83]B. O. Roos, P. Linse, P. E. Siegbahn, and M. R. Blomberg, Chem. Phys. **66**, 197 (1982).
[84]P. Pulay, Int. J. Quantum Chem. **111**, 3273 (2011).
[85]A. Banerjee and J. Simons, Int. J. Quantum Chem. **19**, 207 (1981).
[86]P. Celani, H. Stoll, H. Werner, and P. Knowles, Mol. Phys. **102**, 2369 (2004).
[87]R. F. Fink, Chem. Phys. Lett. **428**, 461 (2006).
[88]R. F. Fink, Chem. Phys. **356**, 39 (2009), moving frontiers in quantum chemistry.
[89]S. Sharma, G. Knizia, S. Guo, and A. Alavi, J. Chem. Theory Comput. **13**, 488 (2017).
[90]P. Celani and H.-J. Werner, J. Chem. Phys. **112**, 5546 (2000).
[91]K. R. Shamasundar, G. Knizia, and H.-J. Werner, J. Chem. Phys. **135**, 054101 (2011).
[92]H. Werner and E. Reinsch, J. Chem. Phys. **76**, 3144 (1982).
[93]H.-J. Werner and P. J. Knowles, J. Chem. Phys. **89**, 5803 (1988).
[94]H.-J. Werner, P. J. Knowles, G. Knizia, F. R. Manby, and M. Schütz, Wiley Interdiscip. Rev.: Comput. Mol. Sci. **2**, 242 (2012).
[95]M. Saitow, Y. Kurashige, and T. Yanai, J. Chem. Phys. **139**, 044118 (2013).
[96]M. Saitow, Y. Kurashige, and T. Yanai, J. Chem. Theory Comput. **11**, 5120 (2015).
[97]M. K. MacLeod and T. Shiozaki, J. Chem. Phys. **142**, 051103 (2015).
[98]K. Sivalingam, M. Krupička, A. A. Auer, and F. Neese, J. Chem. Phys. **145**, 054104 (2016).
[99]J. Planelles, C. Valdemoro, and J. Karwowski, Phys. Rev. A **43**, 3392 (1991).
[100]J. Planelles, C. Valdemoro, and J. Karwowski, Phys. Rev. A **41**, 2391 (1990).
[101]W. Kutzelnigg, J. Chem. Phys. **82**, 4166 (1985).
[102]W. Kutzelnigg and D. Mukherjee, J. Chem. Phys. **107**, 432 (1997).

[103]J. Pipek and P. G. Mezey, J. Chem. Phys. **90**, 4916 (1989).
[104]O. Vahtras, J. Almlöf, and M. Feyereisen, Chem. Phys. Lett. **213**, 514 (1993).
[105]M. Saitow and F. Neese, J. Chem. Phys. **149**, 034104 (2018).
[106]Q. Ma and H.-J. Werner, J. Chem. Theory Comput. **11**, 5291 (2015).
[107]M. Saitow, FEMTO: An Integrated Toolset for the Automated Tensor Generation, Version 0.1.0, https://github.com/msaitow; accessed September 17, 2015.
[108]Y. A. Aoto, A. Bargholz, D. Kats, H.-J. Werner, and A. Köhn, J. Chem. Theory Comput. **15**, 2291 (2019).
[109]We calculated the size-consistency error for an Ne-dimer with an internuclear distance of 1000 Å as E(Ne⋯Ne)–2E(Ne) using def2-SVP and def2-SVP/J auxiliary basis sets. The size-consistency errors caused by CASPT2 and CEPT2 models are 4.03×10^{-5} kcal/mol and 2.04×10^{-5} kcal/mol, respectively.
[110]A. G. Taube and R. J. Bartlett, J. Chem. Phys. **130**, 144112 (2009).
[111]C. L. Janssen and H. F. Schaefer, Theor. Chim. Acta **79**, 1 (1991).
[112]S. Hirata, J. Phys. Chem. A **107**, 9887 (2003).
[113]S. Hirata, J. Chem. Phys. **121**, 51 (2004).
[114]S. Hirata, Theor. Chem. Acc. **116**, 2 (2006).
[115]A. A. Auer, G. Baumgartner, D. E. Bernholdt, A. Bibireata, V. Choppella, D. Cociorva, X. Gao, R. Harrison, S. Krishnamoorthy, S. Krishnan, C.-C. Lam, Q. Lu, M. Nooijen, R. Pitzer, J. Ramanujam, P. Sadayappan, and A. Sibiryakov, Mol. Phys. **104**, 211 (2006).
[116]A. Köhn, J. Chem. Phys. **130**, 104104 (2009).
[117]A. Köhn, J. Chem. Phys. **130**, 131101 (2009).
[118]M. Hanauer and A. Köhn, J. Chem. Phys. **131**, 124118 (2009).
[119]M. Hanauer and A. Köhn, J. Chem. Phys. **134**, 204111 (2011).
[120]J. A. Black and A. Köhn, J. Chem. Phys. **150**, 194107 (2019).
[121]T. Shiozaki, M. Kamiya, S. Hirata, and E. F. Valeev, J. Chem. Phys. **129**, 071101 (2008).
[122]T. Shiozaki, M. Kamiya, S. Hirata, and E. F. Valeev, Phys. Chem. Chem. Phys. **10**, 3358 (2008).
[123]T. Shiozaki, M. Kamiya, S. Hirata, and E. F. Valeev, J. Chem. Phys. **130**, 054101 (2009).
[124]T. Shiozaki, M. Kamiya, S. Hirata, and E. F. Valeev, J. Chem. Phys. **131**, 044118 (2009).
[125]M. Krupička, K. Sivalingam, L. Huntington, A. A. Auer, and F. Neese, J. Comput. Chem. **38**, 1853 (2017).
[126]L. M. J. Huntington, M. Krupička, F. Neese, and R. Izsák, J. Chem. Phys. **147**, 174104 (2017).
[127]A. Sen, B. de Souza, L. M. J. Huntington, M. Krupička, F. Neese, and R. Izsák, J. Chem. Phys. **149**, 114108 (2018).
[128]D. Datta, L. Kong, and M. Nooijen, J. Chem. Phys. **134**, 214116 (2011).
[129]L. Kong, K. R. Shamasundar, O. Demel, and M. Nooijen, J. Chem. Phys. **130**, 114101 (2009).
[130]L. Kong and E. F. Valeev, J. Chem. Phys. **135**, 214105 (2011).
[131]M. Hanrath and A. Engels-Putzka, J. Chem. Phys. **133**, 064108 (2010).
[132]A. Engels-Putzka and M. Hanrath, J. Chem. Phys. **134**, 124106 (2011).
[133]R. Gdanitz and R. Ahlrichs, Chem. Phys. Lett. **143**, 413 (1988).
[134]M. F. Rode and H.-J. Werner, Theor. Chem. Acc. **114**, 309 (2005).
[135]Y. Kurashige, J. Chalupský, T. N. Lan, and T. Yanai, J. Chem. Phys. **141**, 174111 (2014).
[136]M. Hanauer and A. Köhn, J. Chem. Phys. **137**, 131103 (2012).
[137]M. A. Watson and G. K.-L. Chan, J. Chem. Theory Comput. **8**, 4013 (2012).
[138]L. Serrano-Andrés, M. Merchán, I. Nebot-Gil, R. Lindh, and B. O. Roos, The J. Chem. Phys. **98**, 3151 (1993).
[139]D. Zgid, D. Ghosh, E. Neuscamman, and G. K.-L. Chan, J. Chem. Phys. **130**, 194107 (2009).
[140]J. Finley, P.-Å. Malmqvist, B. O. Roos, and L. Serrano-Andrés, Chem. Phys. Lett. **288**, 299 (1998).
[141]T. Shiozaki, W. Győffy, P. Celani, and H.-J. Werner, J. Chem. Phys. **135**, 081106 (2011).
[142]T. Yanai, Y. Kurashige, E. Neuscamman, and G. K.-L. Chan, J. Chem. Phys. **132**, 024105 (2010).
[143]F. Weigend and R. Ahlrichs, Phys. Chem. Chem. Phys. **7**, 3297 (2005).
[144]F. Weigend, Phys. Chem. Chem. Phys. **8**, 1057 (2006).
[145]J. D. Watts, S. R. Gwaltney, and R. J. Bartlett, J. Chem. Phys. **105**, 6979 (1996).
[146]O. Lehtonen, D. Sundholm, R. Send, and M. P. Johansson, J. Chem. Phys. **131**, 024301 (2009).
[147]P. Szalay, A. Karpfen, and H. Lischka, Chem. Phys. **130**, 219 (1989).
[148]M. Dallos and H. Lischka, Theor. Chem. Acc. **112**, 16 (2004).
[149]J. P. Doering and R. McDiarmid, J. Chem. Phys. **73**, 3617 (1980).
[150]L. Serrano-Andrés, M. Merchán, M. Rubio, and B. O. Roos, Chem. Phys. Lett. **295**, 195 (1998).
[151]A. Aspuru-Guzik, O. E. Akramine, J. C. Grossman, and W. A. Lester, J. Chem. Phys. **120**, 3049 (2004).
[152]M. Gouterman and G.-E. Khalil, J. Mol. Spectrosc. **53**, 88 (1974).